remote sensing

MDPI

Article

Is Endmember Extraction a Critical Step in the Analysis of Hyperspectral Images in Mining Environments?

Jingping He *, Dean N. Riley and Isabel Barton

Department of Mining and Geological Engineering, University of Arizona, 1235 James E. Rogers Way, Tucson, AZ 85721, USA; deanriley1@arizona.edu (D.N.R.); fay1@arizona.edu (I.B.)
* Correspondence: jingpinghe@arizona.edu

Abstract: Hyperspectral imaging systems (HSIs) are becoming widespread in the mining industry for mineral classification. The spectral features detectable from near infrared to long-wave infrared make HSIs a potentially efficient tool for exploration, clay mapping, and leach pad modeling. However, the redundancy of hyperspectral data makes the analysis of hyperspectral images complicated and slow. Many researchers have proposed different algorithms and strategies to speed up processing and increase accuracy. These procedures rely on endmember extraction as one of the critical steps. However, no one has tested whether endmember extraction actually improves accuracy under all circumstances. Eliminating endmember extraction, if possible, would speed up the analysis of hyperspectral data. This study tested whether endmember extraction improves the accuracy and efficiency of mapping materials at leach pads, which are among the most complicated situations in mining environments. We compared the accuracy of abundance maps produced with fully constrained least squares (FCLS) (a) with endmember extraction by N-FINDR and (b) without endmember extraction, using a spectral library instead. The results from endmember extraction showed lower accuracy than the results from using a spectral library, probably because the spectral data were noisy and the scanned materials were mixtures. The application of FCLS to hyperspectral images provides useful information for metallurgists. The abundance maps showed that kaolinite, muscovite, and precipitation (hexahydrite and pickeringite) were the dominant minerals on the leach pad. The abundance maps of pipes and precipitation can be used to monitor leaching conditions. Lixiviant ponds mapped out in the abundance map of water can indicate saturation. This technique can also detect organic leakage and agglomeration effectiveness, but it will need different wavelength ranges and more future study. This paper also suggests best practices for using hyperspectral imaging systems to map leach pads.

Keywords: heap leach monitoring; Safford mine; mapping clay minerals; hyperspectral remote sensing; hydrometallurgy; endmember extraction

check for updates

Citation: He, J.; Riley, D.N.; Barton, I. Is Endmember Extraction a Critical Step in the Analysis of Hyperspectral Images in Mining Environments? *Remote Sens.* **2024**, *16*, 2137. https://doi.org/10.3390/rs16122137

Academic Editor: Kamran Esmaeili

Received: 25 April 2024
Revised: 4 June 2024
Accepted: 7 June 2024
Published: 13 June 2024

1. Introduction

1.1. Background and Motivation

Endmember extraction is usually considered a crucial stage in the analysis and classification of hyperspectral images. It involves the extraction of a set of spectral signatures representing the pure endmembers of mixed materials within the scene captured by remote sensing. These endmembers are subsequently used in spectral unmixing algorithms to break down the scene into abundance fractions. Endmember extraction has been widely studied in electrical engineering, remote sensing, information, and computer science. Plaza et al. [1] compared different endmember extraction methods on their simulated and Airborne Visible and Infrared Imaging Spectrometer (AVIRIS) datasets. Veganzones and Grana [2] also summarized different endmember extraction methods and suggested that virtual dimensionality should be used to determine the optimal number of endmembers before endmember extraction.

However, it is not clear whether endmember extraction and related data processing steps are required. Some applications have skipped endmember extraction and directly used general libraries built by the USGS or the JPL and/or ground truth libraries measured on site [3,4]. Figure 1 summarizes these procedures. In this study, the black and red pathways are tested for accuracy. Best practices for HSIs on leach pads are also provided in this paper.

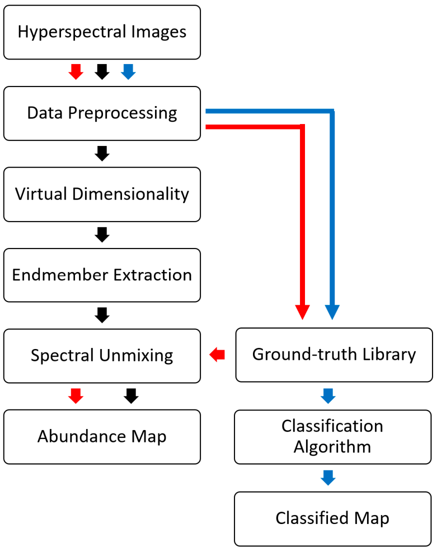

Figure 1. Procedures for analyzing hyperspectral images.

1.2. Background on Leaching and Leach Pad Monitoring

Leaching uses a specific solvent to seep through a pile of stacked ore and dissolve valuable elements. It is an economical method for metallurgical processing of low-grade ores due to its low capital cost and simple technology. It can be applied at different types of mines and is especially widespread in copper mining. Nowadays, 21% of copper is extracted via leaching [5–7].

Mining companies endeavor to monitor and model leach pads through their whole lifespan but are using traditional methods to acquire necessary information such as clay content, P_{80}, raffinate distribution, agglomeration effectiveness, and locations of plugged pipes (Table 1). These traditional methods are easy and cheap. However, the information acquired is discontinuous and inefficient and can be inaccurate, leaving a need for new approaches.

In this paper, an HSI is used to map a heap leach pad to detect lixiviant ponds, clay minerals, precipitation, and irrigation pipes on the leach pad. This has been tried before in [8], in which a spectral angle mapper (SAM) and a ground truth library were used on a leach pad, following the blue pathway in Figure 1. However, there are some drawbacks to this method for classification. For example, the ground truth samples collected on leach pads may not be representative for all the minerals on the leach pads. Additionally, the moisture content and ongoing chemical reactions change the spectra of in situ samples scanned in the lab, and collecting samples on leach pads at different lifts and cells is laborious and unsafe. Furthermore, the pixels of classified maps from a SAM (classification algorithm) are assumed to be pure minerals, but the materials on leach pads are mixtures. Last but not least, this data processing approach does not provide the abundances of the materials, which are important parameters for modeling.

In this paper, we test two more refined, less labor-intensive approaches that can continuously map out several key parameters, listed in in Table 1. Both are based on abundance mapping (data processing method). The parameters mapped are clay content, moisture content to indicate ponding, and sulfate distribution and irrigation pipelines to indicate irrigation status. Traditional methods such as examining Atterberg limits are based on measuring the moisture content to interpret the clay content in samples. Some companies also send samples for X-ray diffraction analysis (XRD) to measure the clay content when they need detailed information about chemical compositions and crystal structures. These methods are time-intensive and in some cases expose people to hazards during sample collection.

Some parameters are not tested, such as P_{80}, the particle size at which 80% of particles by volume are finer. This is usually obtained by sieve analysis. These parameters related with grain size have been left for a future study related to spectral features' depth, width, and asymmetry [9].

As we can see, leach pads [7] are loaded with crushed ores and then irrigated by a lixiviant for a long period, experiencing different chemical reactions and producing precipitates. These make leach pads one of the most complicated situations for remote sensing in mining environments. If processing methods work on leach pads, they should be applicable to all mining situations. This makes leach pads a good test case for the utility of a method in general.

Table 1. The key parameters for modeling leach pads: the current state of the art and perspectives.

Parameters	Current Methods	Suggested Methods
Clay content	Atterberg limits, XRD [10]	Clay abundance map
P_{80}	Sieve screen [11]	Spectral absorption width (future study)
Number of lixiviant ponds	Visual inspection	Water abundance map
Agglomeration status	Visual inspection	Spectral absorption width (future study) Sulfate abundance map
Irrigation pipe status	Visual inspection	Precipitate and pipe map

1.3. Previous Studies of Monitoring Leach Pads

Tang and Esmaeili [12] combined an RGB camera and a thermal infrared (TIR) sensor to monitor the surface moisture on heap leach pads. They acquired images at the El Gallo mine, Mexico, and used two convolutional neural network (CNN) approaches to generate moisture maps. They presented the workflow, from acquiring data to generating the moisture maps, in the paper and concluded that this technique can safely and continuously detect the moisture distribution on leach pads. The results achieved high overall accuracy on the test set but did not yield information such as mineral content, precipitate distribution, and pipeline status.

Daud et al. [13] also used a thermal camera equipped on an unmanned aerial vehicle (UAV) to obtain temperature information on heap leach pads and monitor saturation zones of water. They found the temperature gradient between dry zones and wet zones to be 20 degrees Celsius. They used a Naïve Bayes algorithm to classify heap leach pads into the saturated zone, the irrigated zone, and the dry zone. The thermal images were separated into two sets: one for training and one for evaluation. They concluded that thermal imaging is an efficient method for monitoring the irrigation flow on heap leach pads [13]. Both [12,13] used indirect methods to monitor the moisture content on leach pads.

Zhang and Liu [11] tested an aerial imaging technique to acquire particle size distribution on heap leach pads. They used an RGB camera installed on a drone to take images of bench faces at the Quebrada Blanca copper mine, Chile. After image acquisition, they converted the images into grayscale and calibrated the pixels to real distances in ImageJ. Then, they detected the boundaries of ore particles and measured the sphere diameter in the converted images. They found that the particle size distribution in the Quebrada Blanca leach pads ranged from less than 2 cm to larger than 200 cm in diameter, and finer particles tended to stay at the top of the leach pads. They also put forward that P_{80} was questionable to represent particle size distribution on the leach pads because of its high degree of uncertainty and variability [11]. The ores on leach pads are agglomerated into relatively large sizes, so this method can be used to check the agglomeration effectiveness. However, there are fine contents such as clay minerals on leach pads, which are not detectable by this method.

While not technically remote sensing, Rucker et al. [14] carried out a type of imaging study on a leach pad. They used 12 electrical resistivity geophysical survey lines on a gold leach pad to discern the patterns of high and/or low moisture from past infiltration at the heap leach pad. They found a strong preferential flow where gravity drainage along high permeability channels allows the lixiviant to shortcut to the drainage system and liner. Their data were acquired using a two-dimensional profiling method and integrated into a three-dimensional model. The results showed the distribution of moisture on the leach pad. The dry areas were near the surface and slope angles due to evaporation and capillary barriers. The wet areas were found in the continuous zones, with full connection from top to bottom in the survey areas, which represent preferential flow channeling [14]. This method is widely used and can interpret water retained in the leach pads vertically. However, engineers need to set up survey lines and plugs in the fields for this method, which is laborious and dangerous.

In a review paper, Ren et al. [15] summarized the applications of UAVs equipped with different sensors in mining areas. They concluded that imaging systems can replace traditional measurements and increase efficiency and safety. Ilankoon et al. used different non-invasive techniques to study the flow path visualization pertaining to heap leaching, including positron emission particle tracking (PEPT) [16], electrical capacitance tomography (ECT) [17], ultraviolet (UV) imaging and X-ray computed tomography (XCT) imaging [18]. They tested these high-resolution imaging techniques on packed beds in column leaching, but not at a scale close to heap leaching.

1.4. Hyperspectral Imaging Systems (HSIs)

HSIs have been widely used in different areas such as pharmacology, climate science, agriculture, natural disasters, and food engineering [19–23]. This technology is primarily based on the interaction of light with objects: each photon hits the surface of an object, and its energy will be absorbed, transmitted, emitted, or reflected. Absorption, transmittance, and/or reflectance are determined by the grain size, atoms, and chemical bonds of objects [24]. Hyperspectral sensors can measure the light reflected or emitted from objects and record photons as digital numbers. After that, the digital numbers will be converted into radiance and reflectance (or emittance). The reflectance and/or emittance in specific electromagnetic radiation ranges (wavelengths) is characteristic of each material.

The use of hyperspectral imaging is relatively new for mapping leach pads due to the complexity of data from leach pads, but it has an extensive history of deployment in various mining-related applications. He and Barton [25] used HSIs (drone-based and tripod-based) to detect geotechnically weak areas in mine sites. They used ground truth samples and drill core samples to extract clay minerals' spectra to detect swelling clay in the pit and on the high walls. The study showed that montmorillonite was very concentrated in the weak areas. Other clay minerals such as kaolinite were also detected on the high walls [25].

HSIs have been particularly widely used in mineral exploration, as summarized by Peyghambari and Zhang [26]. They discussed using associated mineral assemblages and spatial alteration patterns to indicate porphyry, epithermal, skarn, volcanic massive sulfide, and iron oxide copper gold deposits. Most of the alteration minerals are distinctive in the visible to near-infrared and short-wave infrared (VNIR–SWIR) (400–2500 nm) and thermal infrared (TIR) (3000–14,000 nm) regions. Bedini [27] and Krupnik and Khan [28] reviewed the literature related to the application of HSIs for mineral exploration and summarized the performance of HSIs in different types of ore deposits. Some other researchers also studied the application of HSIs for mineral classification and mapping acid drainage in mining environments [29–35].

2. Safford Heap Leach Pads

2.1. Location

The testing site was at the Safford mine heap leach pads, located in Graham County, 170 miles east of Phoenix, Arizona. The mine is owned by Freeport-McMoRan Inc. (FMI). Safford is a mine-for-leach operation that produces copper cathode. The operation consists of three open pits, feeding a crushing facility with a design capacity of 103,500 metric tons of ore per day. Safford's copper production totaled 285 million pounds in 2022 [36].

2.2. Rock Types and Minerals in the Area

Robinson and Cook [37] studied this area and mentioned that there are at least five porphyry copper deposits in the Safford district: Dos Pobres, San Juan, Kennecott, Sanchez, and Lone Star (Figure 2). FMI previously mined oxide minerals from Dos Pobres and San Juan and is currently mining Lone Star. However, the minerals in the scanning area are mainly from Dos Pobres. Langton and Williams [38] studied the mineralization and alteration in this area. The principal rock types of the Dos Pobres orebody are Safford Metavolcanics, the Productive Porphyries, hornblende andesite dikes and sills, and the Baboon Metavolcanics. The principal ore minerals are chrysocolla, Cu-bearing iron oxides, and supergene sulfides.

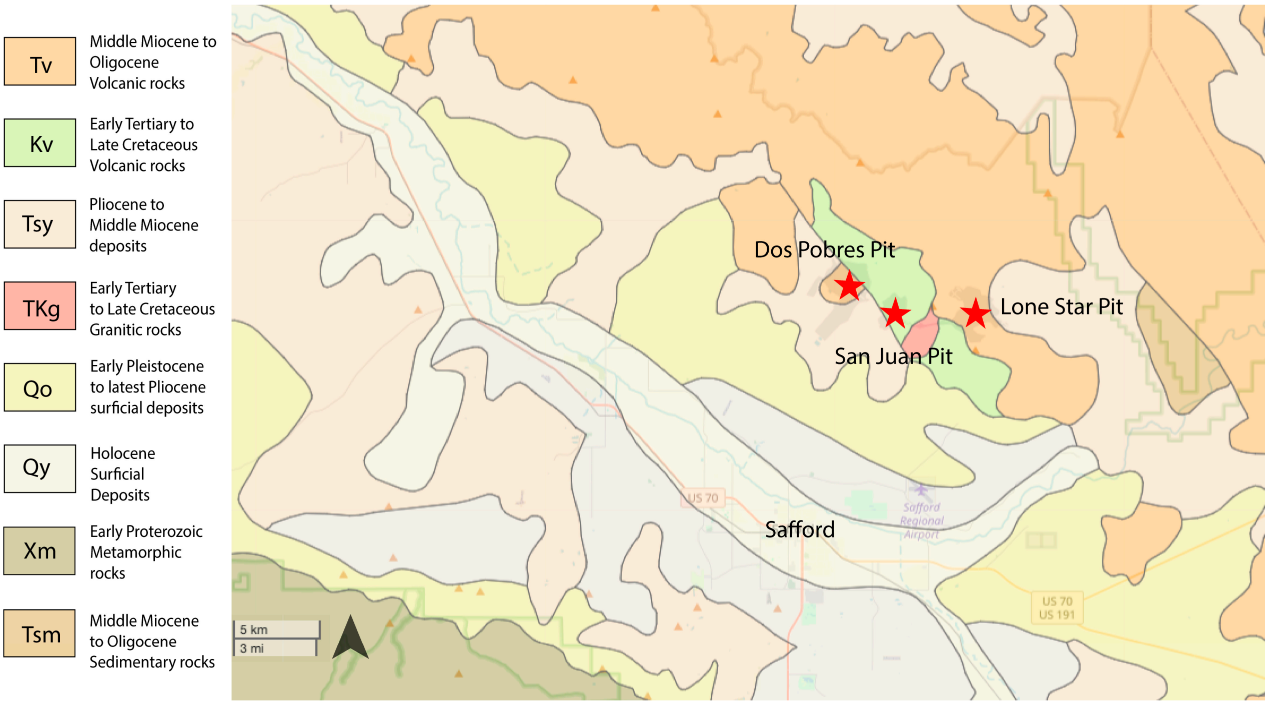

Figure 2. Simplified geologic map of the Safford district, from [39]. Arrow indicates north.

2.3. Lithologies Materials on the Leach Pad

Table 2 summarizes the rock units, minerals, and their corresponding spectral features at the Dos Pobres orebody.

The ores on the leach pads are mainly from the Safford Metavolcanics and the Productive Porphyries. Feldspar, quartz, biotite, amphibole, muscovite, epidote, kaolinite, gypsum, pyroxene, chlorite, calcite, pyrite, chalcopyrite, and chrysocolla may occur in the scanning area. The wavelength range used in this study is 980–2400 nm (SWIR) because the critical features of possible minerals on the scanned leach pad are in this spectral region. Table 3 shows the possible mineral groups in the scanning area and their corresponding spectrally active ranges. Some minerals are spectrally inactive in our study range, such as feldspar, which is active in the long-wave infrared (LWIR) region but lacks VNIR and

SWIR features. Thus, some minerals, such as quartz and feldspar, are dominant in the ores but not in the spectra.

Table 2. Rock types and their corresponding compositions, minerals, and spectral features at Dos Pobres orebody [26,27,38,40]. Only the spectral features of spectrally active minerals are discussed.

Rock Type	Composition	Minerals	Spectral Features
Gila Mountain Volcanics	Basalt and rhyolite dikes, sills, plugs, basalt flows, tuffs, rhyolites, agglomerates, vent debris, basal conglomerate	Plagioclase, pyroxene *, quartz, potassium feldspar, hornblende, biotite *	Pyroxene: 702 nm, 900 nm, 1040 nm (VNIR) Amphibole: 1400 nm, 2320~2330 nm, 2390~2400 nm (SWIR) Biotite: 900 nm, 1165 nm (VNIR), 2240–2256 nm, 2320~2360 nm, 2380 nm (SWIR)
Baboon Metavolcanics-Metavolcaniclastics	Hornblende andesite dikes, sills, plugs Propylitized andesite agglomerates, flow breccias, mud flows, lithic tuffs, conglomerates	Plagioclase, hornblende *, pyroxene *, biotite *, pennine (chlorite) #, epidote #, calcite #, muscovite #	Pyroxene: 702 nm, 900 nm, 1040 nm (VNIR) Amphibole: 1400 nm, 2320~2330 nm, 2390~2400 nm (SWIR) Biotite: 900 nm, 1165 nm (VNIR), 2240–2256 nm, 2320~2360 nm, 2380 nm (SWIR) Muscovite: 1410 nm, 2114 nm, 2180~2228 nm, 2342 nm, 2435 nm (SWIR) Mg-Chlorite: 1394 nm, 1430 nm, 1506 nm, 1880 nm, 1980 nm, 2245 nm, 2325 nm, 2380 nm (SWIR) Epidote: 1830 nm, 1947 nm, 2256 nm, 2335~2342 nm (SWIR) Calcite: 1880 nm, 1992 nm, 2156 nm, 2340~2345 nm (SWIR)
Productive Porphyries	Tonalite-quartz monzonite-monzonite-granodiorite porphyry stock(s), dikes, and sills	Plagioclase, quartz, orthoclase, hornblende *, biotite #, magnetite, bornite, epidote #, chlorite #, muscovite #, kaolinite #, carbonate #, gypsum #	Amphibole: 1400 nm, 2320~2330 nm, 2390~2400 nm (SWIR) Muscovite: 1410 nm, 2114 nm, 2180~2228 nm, 2342 nm, 2435 nm (SWIR) Kaolinite: 1400 nm, 1412 nm, 1830 nm, 2162 nm, 2206 nm, 2312 nm, 2350 nm, 2380 nm (SWIR) Biotite: 900 nm, 1165 nm (VNIR), 2240–2256 nm, 2320~2360 nm, 2380 nm (SWIR) Epidote: 1830 nm, 1947 nm, 2256 nm, 2335~2342 nm (SWIR) Fe-Chlorite: 2261 nm, 2355~2365 nm (SWIR) Mg-Chlorite: 1394 nm, 1430 nm, 1506 nm, 1880 nm, 1980 nm, 2245 nm, 2325 nm, 2380 nm (SWIR) Calcite: 1880 nm, 1992 nm, 2156 nm, 2340~2345 nm (SWIR) Gypsum: 1449 nm, 1490 nm, 1535 nm, 1750 nm, 1948 nm, 2215 nm

Table 2. *Cont.*

Rock Type	Composition	Minerals	Spectral Features
Lone Star Pluton (s)	Quartz diorite-granodiorite batholith	Plagioclase, quartz, potassium feldspar, hornblende *, biotite *	Amphibole: 1400 nm, 2320~2330 nm, 2390~2400 nm (SWIR) Biotite: 900 nm, 1165 nm (VNIR), 2240–2256 nm, 2320~2360 nm, 2380 nm (SWIR)
Safford Metavolcanics-Metavolcaniclastics	Metamorphosed hornblende and pyroxene andesite flow, breccias, agglomerates, wackes, and mud flows	Plagioclase, quartz, orthoclase, hornblende *, biotite #, magnetite, bornite, epidote #, chlorite #, muscovite #, kaolinite #, carbonate #	Pyroxene: 702 nm, 900 nm, 1040 nm (VNIR) Amphibole: 1400 nm, 2320~2330 nm, 2390~2400 nm (SWIR) Biotite: 900 nm, 1165 nm (VNIR), 2240–2256 nm, 2320~2360 nm, 2380 nm (SWIR) Muscovite: 1410 nm, 2114 nm, 2180~2228 nm, 2342 nm, 2435 nm (SWIR) Kaolinite: 1400 nm, 1412 nm, 1830 nm, 2162 nm, 2206 nm, 2312 nm, 2350 nm, 2380 nm (SWIR) Epidote: 1830 nm, 1947 nm, 2256 nm, 2335~2342 nm (SWIR) Fe-Chlorite: 2261 nm, 2355~2365 nm (SWIR) Mg-Chlorite: 1394 nm, 1430 nm, 1506 nm, 1880 nm, 1980 nm, 2245 nm, 2325 nm, 2380 nm (SWIR) Calcite: 1880 nm, 1992 nm, 2156 nm, 2340~2345 nm (SWIR)

* Spectrally active minerals in VNIR/SWIR; # altered minerals.

Table 3. The spectrally active ranges of possible minerals in the scanning area [41].

Mineral Group	Example	VNIR	SWIR	LWIR
Amphibole	Hornblende	None	Good	Moderate
Pyroxene	Diopside	Good	Moderate	Good
Epidote	Epidote	None	Good	Moderate
Mica	Muscovite	None	Good	Moderate
Chlorite	Clinochlore	None	Good	Moderate
Clay Minerals	Kaolinite	None	Good	Moderate
Feldspar	Orthoclase	None	None	Good
Sulfate	Gypsum	None	Good	Moderate
Carbonate	Calcite	None	Moderate	Good
	Hematite	None	None	None
	Pyrite	None	None	None

3. Methods

3.1. Spectral Library

The spectral library used in this study consists of two parts. One part is from the USGS mineral library, which includes kaolinite, muscovite, biotite, chlorite, epidote, hornblende, enstatite, water + swelling clay, and montmorillonite. The other part is from ground truth samples taken during field work, including irrigation pipes and precipitates. To make the reference spectra consistent in the library, the irrigation pipes and precipitates were scanned using an ASD TerraSpec analyzer at the University of Arizona in Tucson, Arizona. The precipitates were identified as hexahydrite ($MgSO_4 \cdot 6H_2O$) and pickeringite ($MgAl_2(SO_4)_4 \cdot 22H_2O$) by XRD analysis performed by ALS Global. The reference spectra are shown in Figure 3.

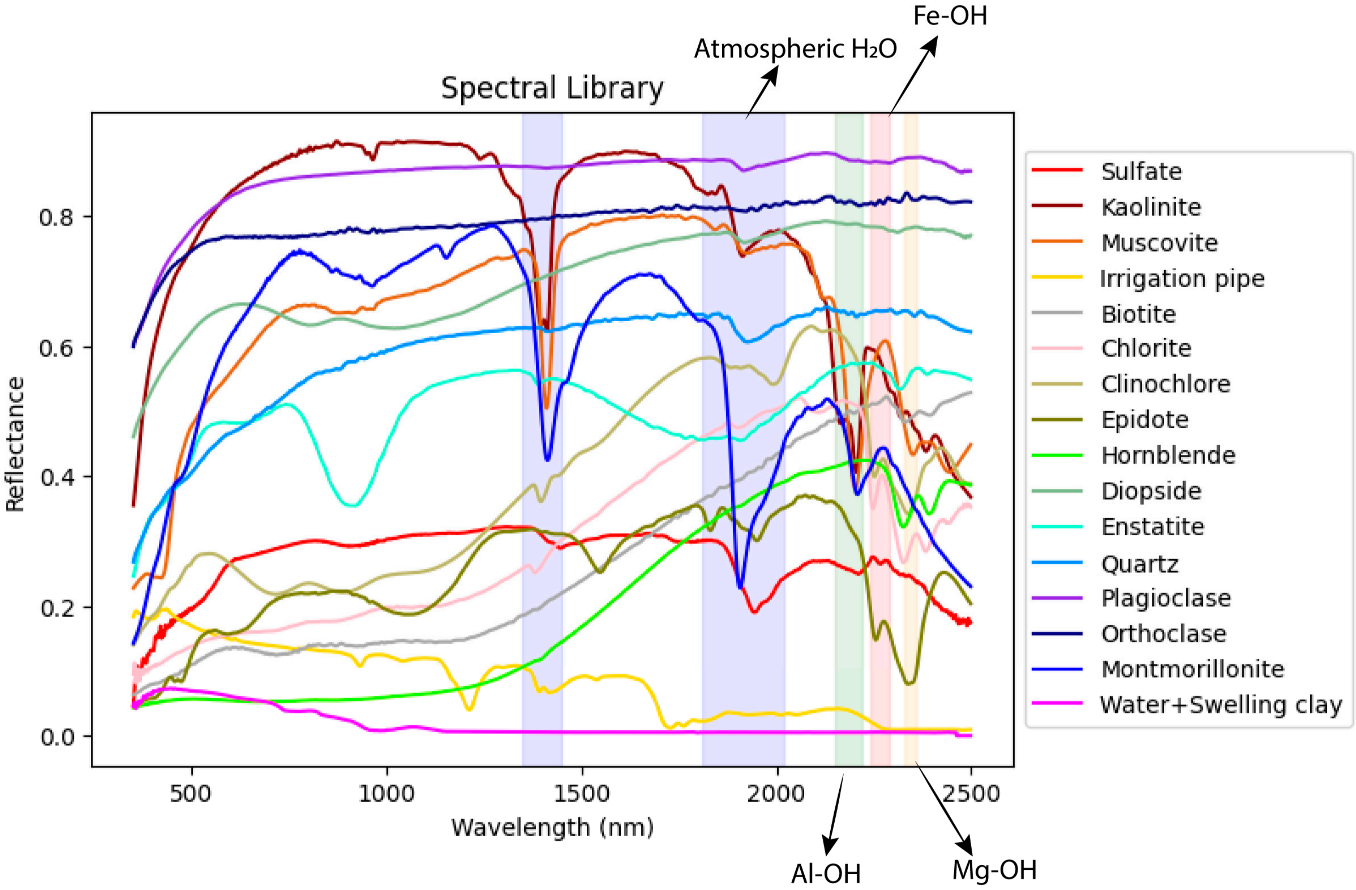

Figure 3. The reference spectra selected from the USGS library and the ground truth spectra (sulfate and irrigation pipe). Atmospheric H_2O absorption feature regions are in blue. Al-OH, Fe-OH, and Mg-OH absorption feature regions are in green, brown, and orange, respectively.

3.2. Data Acquisition and Preprocessing

The HSI used in this study is a coaligned VNIR/SWIR sensor from Headwall Photonics, a push broom scanner with a range of 400–2500 nm including 270 bands for VNIR and 170 bands for SWIR. It was flown on a DJI UAV system (Matrice 600 Pro). A global positioning system was attached on the drone so hyperspectral images were georeferenced. The flight paths were designed before the scanning by pilots from Headwall Photonics, and cooling pads were used to reduce the effect of temperature on the sensor. Black and white tiles and a Spectralon tarp were set on the leach pad and used as calibration references in the scene. The flight was completed on a sunny day (10:00 a.m.–4:00 p.m.) in September 2019. The flight elevation was 40 m and the pixel size was 8 cm^2. The spectral resolution in SWIR was 9 nm. Figure 4 shows the true color RGB mosaic of the HSI data on the leach pad. The gap in the image was caused by the mosaicking of data from the VNIR flightline, so it will not cause problems for our study (SWIR). The brown materials are crushed ores and white lines are precipitates on the leach pad. The horizontal striping was also caused by mosaicking. Smaller, curved striping through the image is due to the ore stacker.

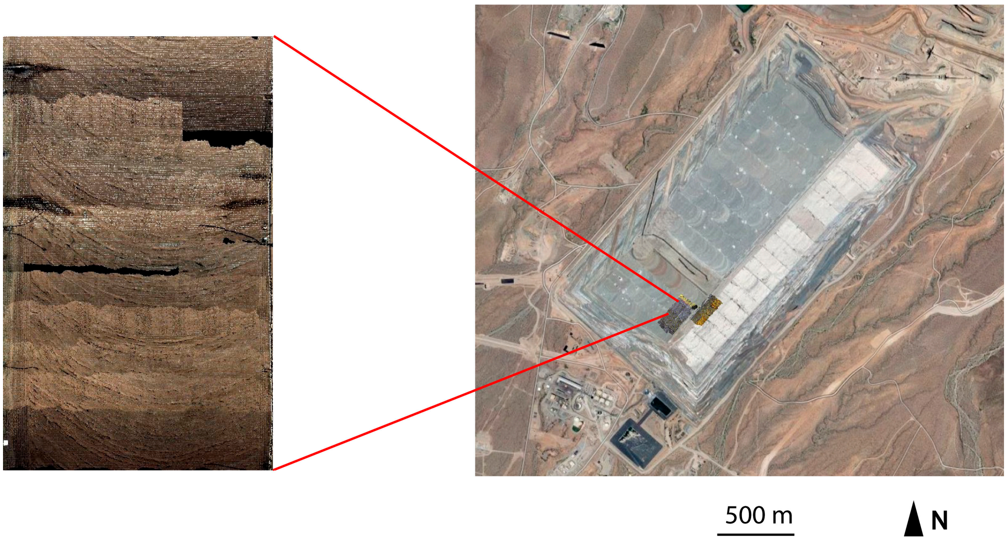

Figure 4. True color RGB mosaic of the leach pad.

After data acquisition, Headwall Photonics converted the digital numbers to radiance and then to reflectance, which was summarized by Barreto and others [42]. After data calibration, a Savitzky–Golay filter [43] was used to smooth the data, with filter widths set at 5 and degree of smoothing polynomial set at 4.

3.3. Spectral Class Selection

Principal component analysis (PCA) is a method for reducing the dimensionality of data. It was used for testing virtual dimensionality, which is a procedure to determine the number of endmembers. When N-FINDR (which will be illustrated below) extracts endmembers, the dimensionality of data is reduced based on the number of endmembers input. If the number input is too small, the data reduction will cause a severe loss of spectral information. This can indicate the minimum number of endmembers needed for this study. PCA was originally used for statistics by Pearson [44] but has been applied to the analysis of hyperspectral images, as summarized by Rodarmel and Shan [45]. The original data were transformed to remove the correlation among the bands. The results can be visualized as the subtraction of spectra between extreme differences within the dataset. The "elbow" joint in the PCA scree plot indicates the minimum number of endmembers that are needed for the dataset.

HySime [46] is the second method tested in this study for virtual dimensionality. This method selects the subset of eigenvectors that best represents the signal subspace in the minimum mean square error sense. It minimizes the mean square error based on two terms. One term corresponds to the power of the signal projection error and is a decreasing function of the subspace dimension; the second term corresponds to the power of noise projection and is an increasing function of subspace dimension. HySime increases the dimension until the mean square error reaches the optimal point.

3.4. N-FINDR

We used N-FINDR to determine the spectra of endmembers in the scene [47]. It tries different spectra in the hyperspectral images and calculates the volume of the endmember matrix based on the following formula:

$$\mathrm{V}(\mathbf{E}) = \frac{1}{(1-1)!}\mathrm{abs}(|\mathbf{E}|) \tag{1}$$

where **E** is the matrix of endmembers augmented with a row of ones:

$$\mathbf{E} = \begin{bmatrix} 1 & \cdots & 1 \\ \vec{e}_1 & \cdots & \vec{e}_l \end{bmatrix} \tag{2}$$

where $\vec{e}$ is a column vector representing a pixel's spectrum and is the reference spectrum extracted from the hyperspectral image of the leach pad; **E** is a group of reference spectra ($\vec{e}$); V is the volume, which is proportional to the determinant of **E**; and l represents the number of endmembers. The algorithm will choose the group of spectra with the highest volume as endmembers. In our study, the input to the N-FINDR algorithm is the hyperspectral image of the leach pad.

3.5. Fully Constrained Least Squares

Fully constrained least squares (FCLS) linear unmixing was used to generate the abundance map. It was derived from an unconstrained least squares unmixing and based on orthogonal subspace projection [48]. We assume **r** is a $p \times 1$ vector representing a pixel in a hyperspectral image, p is the number of spectral bands, and **M** is a $p \times n$ endmember matrix (signature matrix).

$$\mathbf{M} = (\mathbf{m}_1, \mathbf{m}_2, \cdots, \mathbf{m}_\mathrm{n})$$

where $\mathbf{m}_\mathrm{n}$ is the vector representing the nth endmember for classification. Let $\boldsymbol{\alpha}$ be the $n \times 1$ abundance vector:

$$\boldsymbol{\alpha} = (\alpha_1, \alpha_2, \cdots, \alpha_\mathrm{n})^\mathrm{T}$$

The linear regression model of **r** can be represented as follows:

$$\mathbf{r} = \mathbf{M}\boldsymbol{\alpha} + \xi,$$

where ξ is a $p \times 1$ vector representing additive Gaussian noise with zero mean and variance $\sigma^2\mathbf{I}$. After least squares error, the least squares estimate of the unconstrained linear unmixing model is the following:

$$\hat{\alpha} = \left(\mathbf{M}^T\mathbf{M}\right)^{-1}\mathbf{M}^T\mathbf{r}$$

FCLS is based on the unconstrained method with an added Lagrange multiplier to constrain $\boldsymbol{\alpha}$ to 1. In order to make the calculation easier, the new constrained least squares linear unmixing problem is as follows:

$$J = \frac{1}{2}(\mathbf{r} - \mathbf{M}\boldsymbol{\alpha})(\mathbf{r} - \mathbf{M}\boldsymbol{\alpha})^T - \lambda(\sum_{j=1}^{n} \alpha_j - 1)$$

where $\frac{1}{2}(\mathbf{r} - \mathbf{M}\boldsymbol{\alpha})(\mathbf{r} - \mathbf{M}\boldsymbol{\alpha})^T$ is the original unconstrained least squares problem and adding ½ is to make differentiating easier; λ is the multiplier; $(\sum_{j=1}^{n} \alpha_j - 1)$ is the constraint function, which constrains the sum of α_j to 1; **M** represents the group of reference spectra from the hyperspectral image of the leach pad, which was extracted by N-FINDR and equals **E** in Equation (1); **r** represents any unknown pixel in the hyperspectral image; and $\boldsymbol{\alpha}$ is a parameter that scales the endmembers and represents the abundance of endmembers in unknown pixels.

4. Results

4.1. Virtual Dimensionality Results

Figure 5 is the scree plot for the dataset. It shows that component 3 is the "elbow" joint, and the cumulative percentage variance of the first four components goes up to 90%. This indicates that at least five endmembers are needed from N-FINDR, because during the endmember extraction, the data will be transformed and compressed by a minimum noise fraction (MNF), which reduces the image dimensionality to one less than the number of endmembers [47]. If the dimensionality of the transformed image is less than four, the information will be lost.

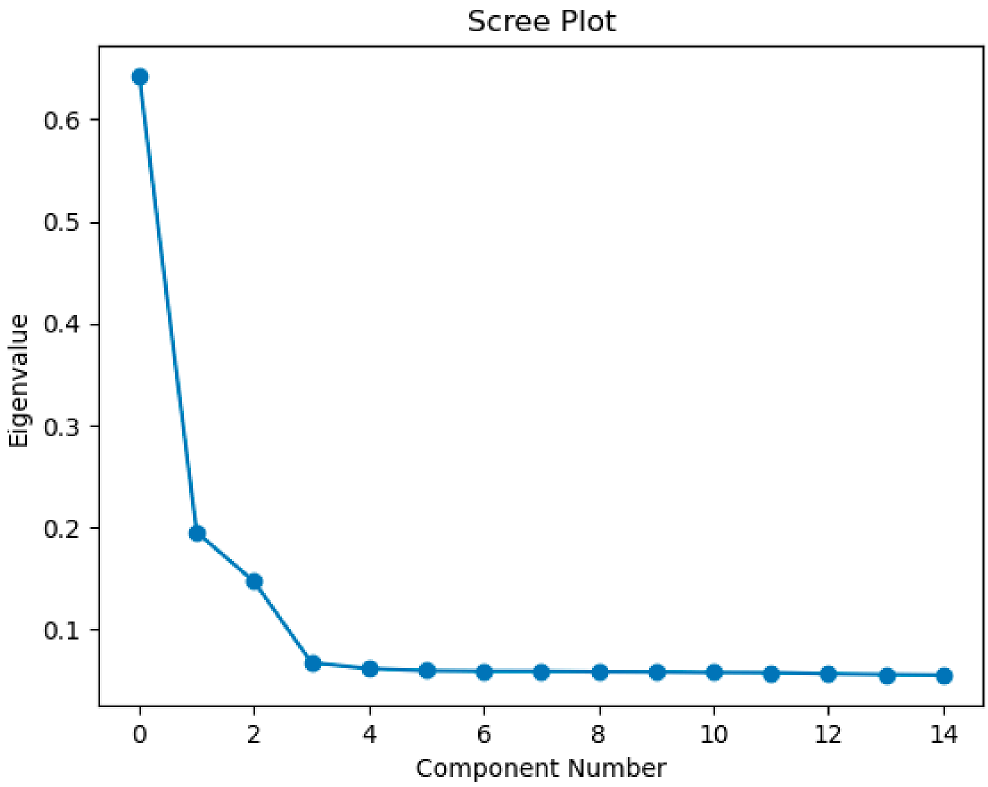

Figure 5. Scree plot for hyperspectral data on leach pad (based on PCA).

HySime was tested before and after applying the Savitzky–Golay filter. The virtual dimensionalities were 8 and 1, respectively. We discounted the second HySime result because one endmember on a leach pad is unrealistic. As Table 3 shows, there were eight SWIR-active mineral groups in the leach pad, plus irrigation pipes and water. Therefore, we chose 10 endmembers for the analysis.

4.2. N-FINDR Results

Figure 6 shows the results of N-FINDR with 10 endmembers.

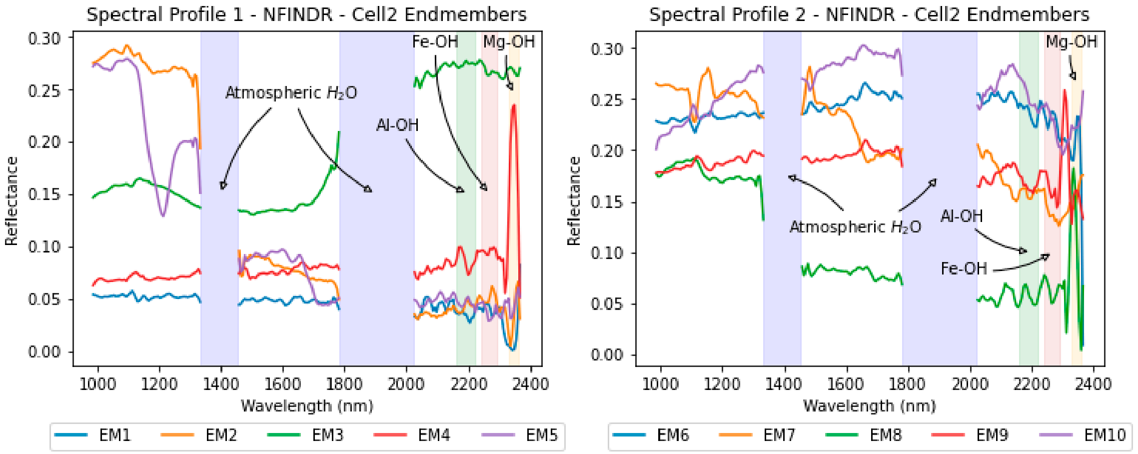

Figure 6. The 10 endmembers of the input hyperspectral image. Atmospheric H_2O absorption feature regions are in blue. Al-OH, Fe-OH, and Mg-OH absorption feature regions are in green, brown, and orange, respectively.

Table 4 shows the results of FCLS unmixing of each of the 10 endmembers.

Table 4. The components of the endmembers extracted from N-FINDR.

	EM1	**EM2**	**EM3**	**EM4**	**EM5**	**EM6**	**EM7**	**EM8**	**EM9**	**EM10**
Sulfate	0%	0%	0%	0%	0%	38%	0%	0%	31%	52%
Kaolinite	1%	0%	0%	0%	0%	5%	15%	0%	0%	0%
Muscovite	1%	0%	0%	0%	0%	0%	0%	0%	4%	2%
Irrigation pipe	4%	87%	0%	0%	90%	3%	52%	61%	0%	0%
Biotite	0%	0%	34%	8%	0%	0%	0%	0%	1%	0%
Chlorite	0%	0%	0%	0%	0%	17%	0%	0%	0%	0%
Clinochlore	0%	0%	0%	0%	0%	0%	0%	0%	0%	16%
Epidote	3%	0%	0%	0%	0%	0%	0%	0%	0%	5%
Hornblende	0%	0%	0%	0%	0%	0%	0%	0%	0%	0%
Diopside	0%	0%	0%	0%	0%	0%	0%	0%	7%	0%
Enstatite	0%	0%	15%	6%	0%	4%	11%	0%	0%	0%
Quartz	0%	0%	0%	0%	0%	0%	0%	0%	0%	0%
Plagioclase	0%	0%	0%	0%	0%	0%	0%	0%	0%	0%
Orthoclase	0%	0%	0%	3%	0%	0%	0%	0%	0%	0%
Montmorillonite	2%	13%	0%	0%	10%	0%	0%	11%	1%	2%
Water + swelling clay	88%	0%	51%	84%	0%	32%	22%	28%	56%	24%

5. Discussion

5.1. PCA

According to the PCA results, the hyperspectral dataset indeed acquired some useful information related to the parameters in Table 1. Figure 7 shows three components' images from PCA, which emphasize the variance within the data acquired from leach pad. In the first component image, the light colored pixels are distributed in arc shapes, which indicates that this component is highly related to minerals. It shows how ores were loaded by stackers. The irrigation pipe features were captured by the third component and are shown as horizontal lines. Figure 8 is a zoomed version of the third component image of the same dataset. The second component image highlights the differences between the flight lines.

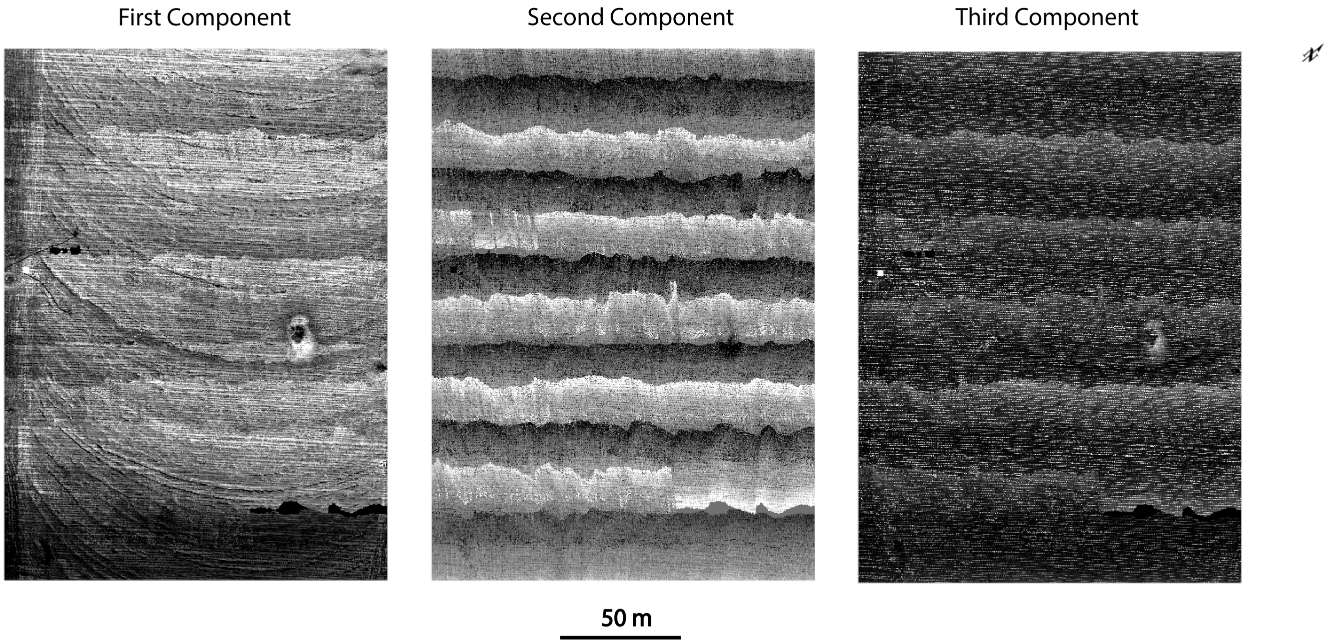

Figure 7. The three components' images from PCA.

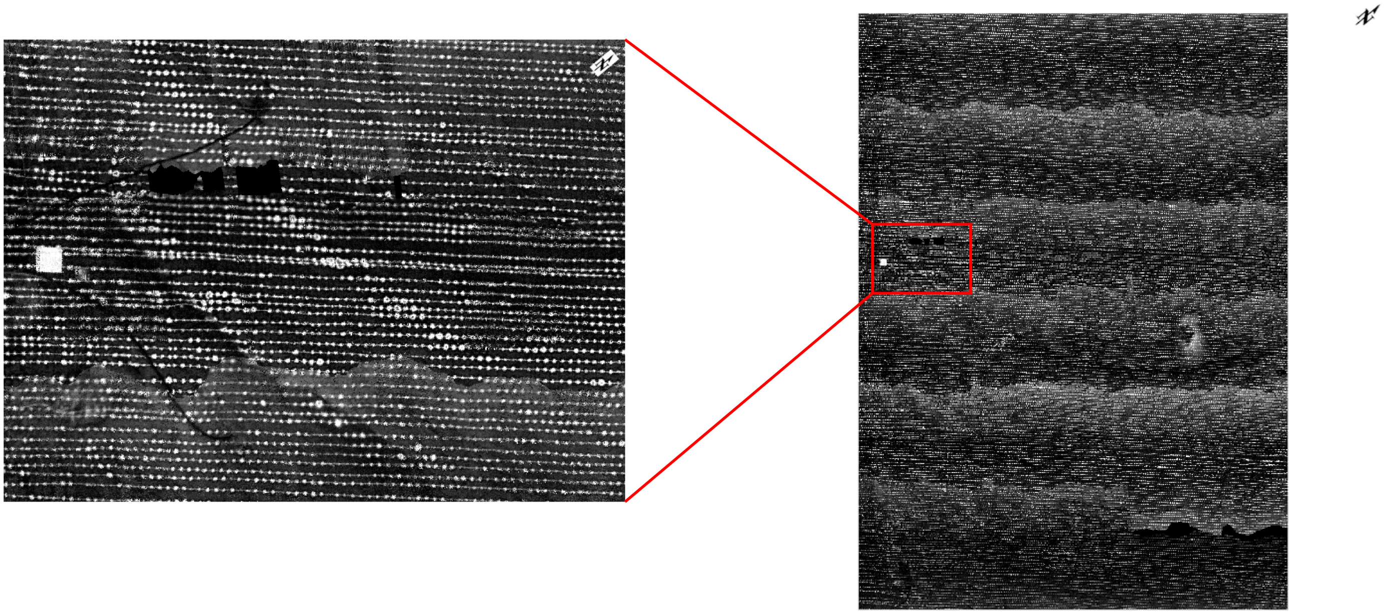

Figure 8. Close-up of part of the third component of the PCA image (Figure 7).

5.2. Virtual Dimensionality

Virtual dimensionality is a popular method to decide the number of endmembers, but it did not work on this dataset. PCA revealed that there are at least five endmembers before smoothing and at least three endmembers after smoothing. HySime showed that eight endmembers are needed before smoothing and only one endmember is needed after smoothing, which is unrealistic.

There are many reasons why virtual dimensionality does not work on our dataset. The methods rely on variances between spectra, but smoothing reduces the variance. However, smoothing is necessary because otherwise the variance of noise will be treated as features. After smoothing, the suggested numbers of endmembers were lower than the number expected. This was probably due to moisture dampening the reflectance and the homogenizing effect from the crushed, mixed, agglomerated, and irrigated ores. HySime treated all the smoothed spectra as one kind.

5.3. Endmembers and Their Abundance Maps

The endmembers were extracted by N-FINDR and unmixed by a library (Figure 3). In Figure 5, the reflectance of all endmembers is very low, at less than 30%. That is because all the ores on the leach pad were wet during the scanning. This is consistent with a study from Tian and Philpot [49], who compared saturated soil samples and dry counterparts and found that soil water decreased reflectance. The spectra showed only a few strong features of minerals in wet soils.

EM1 is most likely water (Table 4). It was detected all over the leach pad (Figure 9) and was especially abundant in lixiviant ponds. According to the abundance map, the water content accounts for 60–80%, which is highly suspicious. Figure 9 also shows some gaps between flight lines, identified as EM1. The plot shows that the reflectance of EM1 is lower than 5%, except for the noise after 2300 nm. Therefore, EM1 was interpreted as a mixture of water and background.

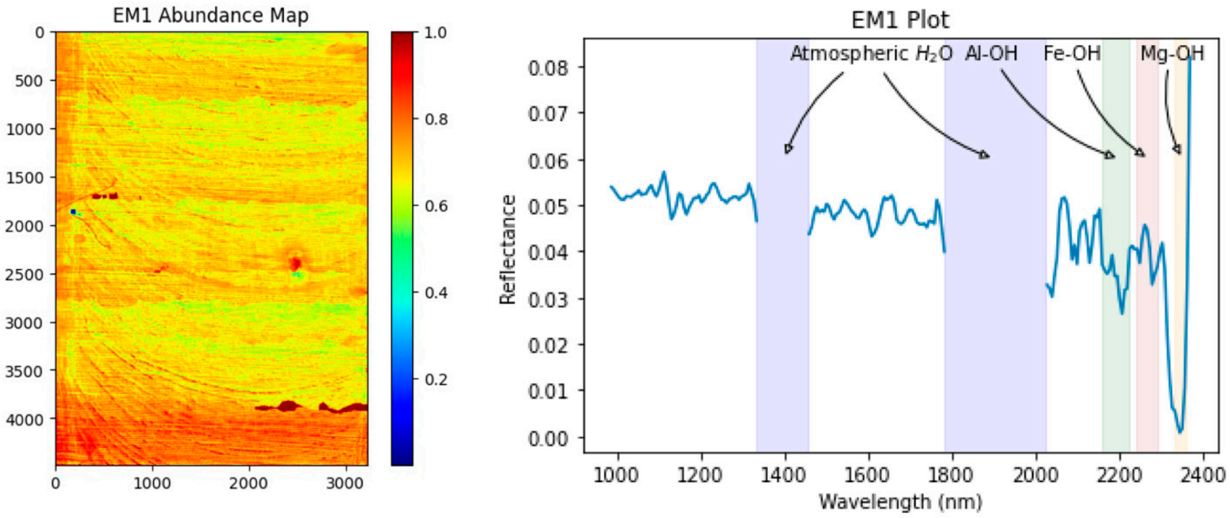

Figure 9. The spatial distribution of EM1 (**left**). Plot of the spectrum (EM1) from NFINDR (**right**). Atmospheric H_2O absorption feature regions are in blue. Al-OH, Fe-OH, and Mg-OH absorption feature regions are in green, brown, and orange, respectively.

EM2 was identified as mostly irrigation pipe (Table 4). The horizontal lines are irrigation pipes on the leach pad (Figure 10). The plastic features we detected near 1100 nm and 1200 nm correspond to the wavelengths found by Moshtaghi et al. [50] at 1070 nm, 1214 nm, and 1729 nm. In our study, the feature at 1729 nm is very weak due to the mixture of minerals, water, and pipes in one 8 cm^2 pixel. There is a little montmorillonite in EM2 as well. Montmorillonite is a type of swelling clay and has a distinctive feature at 2205–2212 nm related to Al-OH absorption [40]. In the abundance map of EM2 (Figure 10), montmorillonite is concentrated around ponds. Montmorillonite can cause lixiviant ponding because swelling clay can absorb water and expand to reduce permeability.

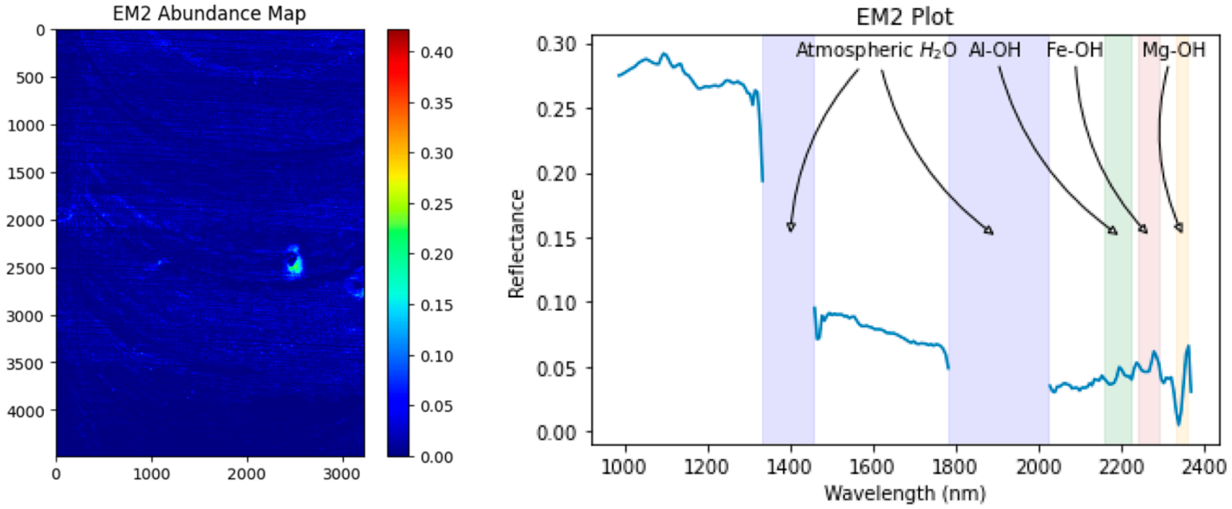

Figure 10. The spatial distribution of EM2 (**left**). Plot of the spectrum (EM2) from NFINDR (**right**). Atmospheric H_2O absorption feature regions are in blue. Al-OH, Fe-OH, and Mg-OH absorption feature regions are in green, brown, and orange, respectively.

EM3 represents a type of soaked mineral mixture (biotite and enstatite) on leach pads (Table 4). The minerals are distributed along the stacking traces in Figure 11. The biotite spectrum has a double feature at 2255 nm and 2350~2360 nm. The feature at 2255 nm is the diagnostic Fe-OH absorption and the feature at 2350~2360 nm is the diagnostic Mg-OH absorption. Enstatite is a type of orthopyroxene which has a wide feature from 1400 nm to 2100 nm and a sharp feature near 900 nm [40]. The identification of enstatite is suspect because it is not consistent with the mineralogy at Safford (Table 2). It could be diopside, which is also a pyroxene and shares some similar features.

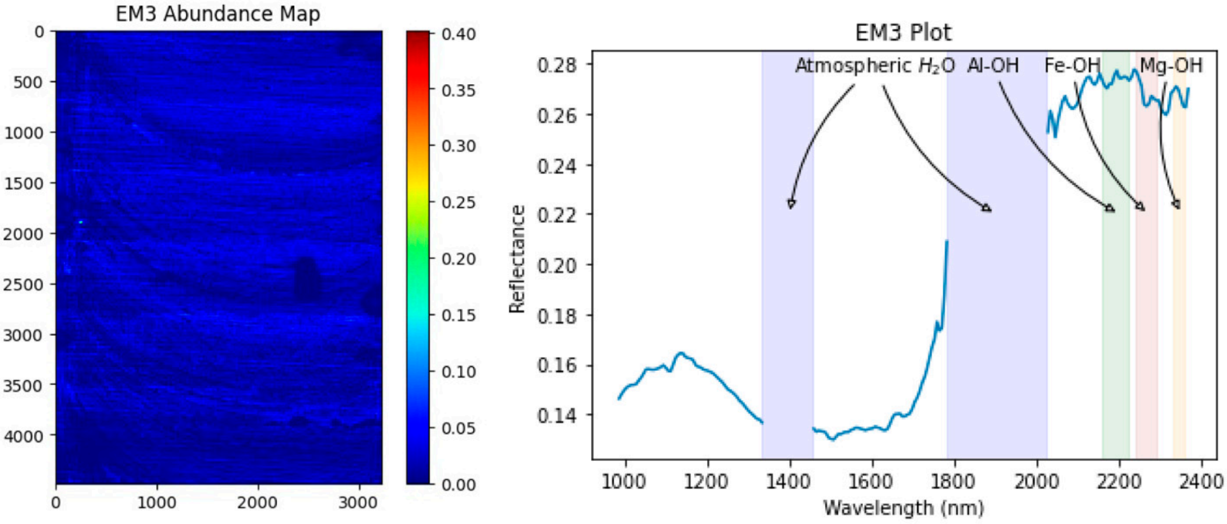

Figure 11. The spatial distribution of EM3 (**left**). Plot of the spectrum (EM3) from NFINDR (**right**). Atmospheric H_2O absorption feature regions are in blue. Al-OH, Fe-OH, and Mg-OH absorption feature regions are in green, brown, and orange, respectively.

EM4 is similar to EM3 in distribution but includes a higher moisture content (Table 4). That is why the average reflectance of EM4 is lower than that of EM3 and the abundance of EM4 is higher than that of EM3 (Figure 12). The spike at 2350 nm is not a mineral feature and is most likely noise or caused by artificial problems.

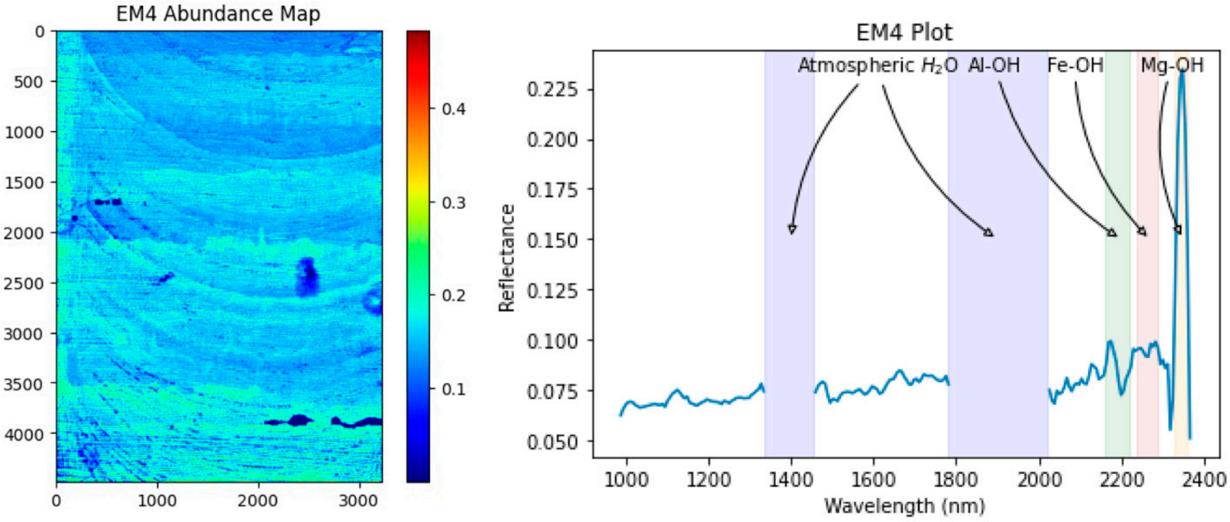

Figure 12. The spatial distribution of EM4 (**left**). Plot of the spectrum (EM4) from NFINDR (**right**). Atmospheric H_2O absorption feature regions are in blue. Al-OH, Fe-OH, and Mg-OH absorption feature regions are in green, brown, and orange, respectively.

EM5 is similar to EM2, and the horizontal pipelines are very clear in Figure 13. However, EM5 has stronger plastic features at 1070 nm, 1214 nm, and 1729 nm and weaker montmorillonite features.

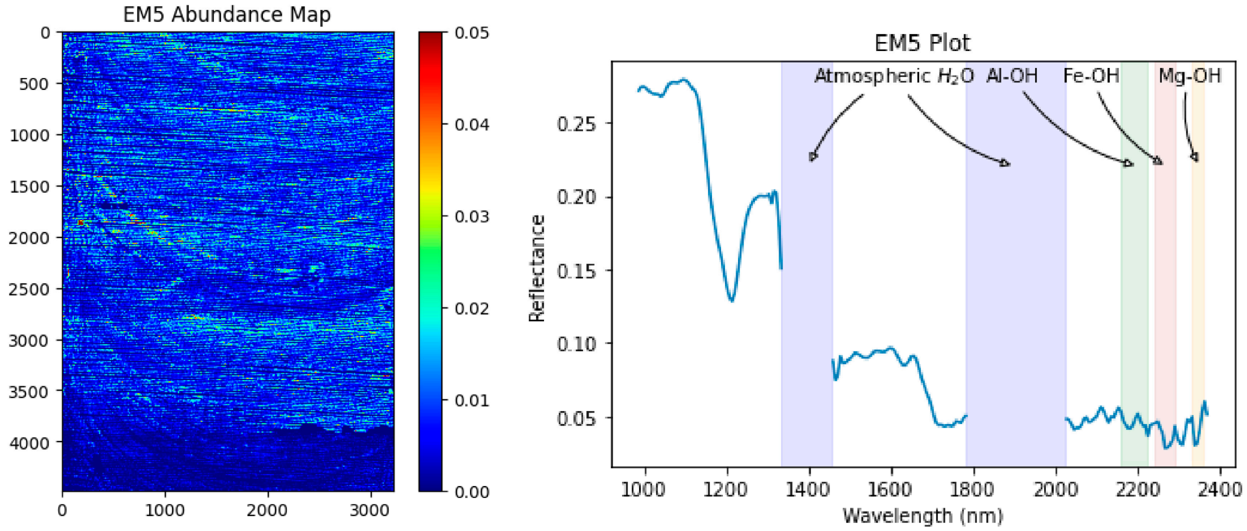

Figure 13. The spatial distribution of EM5 (**left**). Plot of the spectrum (EM5) from NFINDR (**right**). Atmospheric H_2O absorption feature regions are in blue. Al-OH, Fe-OH, and Mg-OH absorption feature regions are in green, brown, and orange, respectively.

EM6 was identified as a mixture of chlorite and sulfate precipitate. Cloutis et al. [51] studied sulfates and found that they have similar spectral features near 1440–1460 nm, 1930–1950 nm, and 1970 nm. In this study, a weak feature at 1460–1500 nm and a triple weak feature at 2150–2250 nm were detected. Chlorite has a diagnostic Fe-OH absorption at 2245 nm. Mg-rich chlorite also has a deep feature at 2325 nm. Sometimes, as shown in Figure 14, this feature is a doublet, representing a high proportion of Mg. The drop feature after 2350 nm is noise.

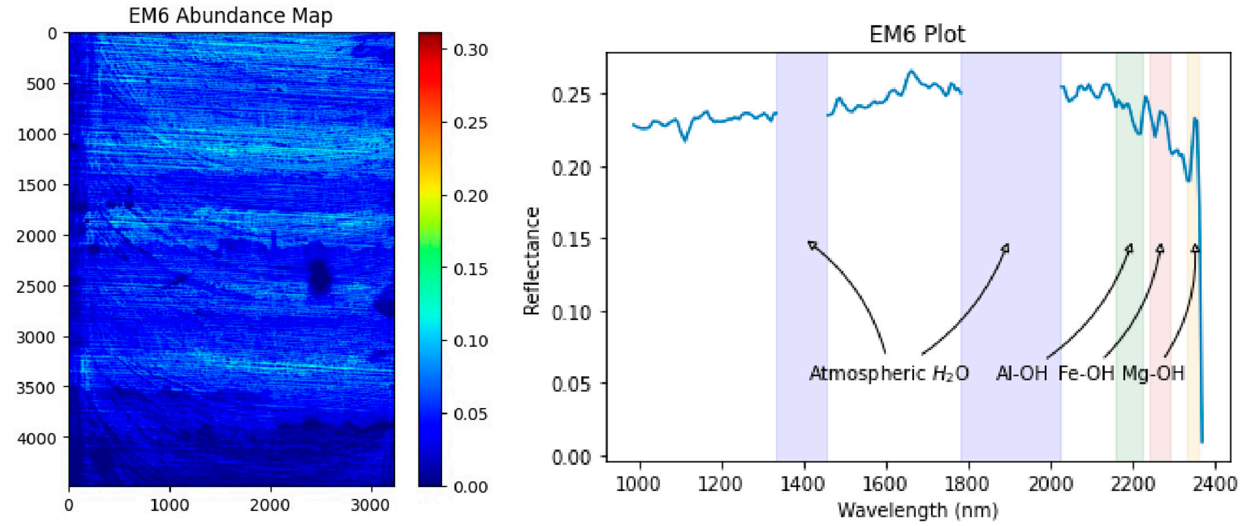

Figure 14. The spatial distribution of EM6 (**left**). Plot of the spectrum (EM6) from NFINDR (**right**). Atmospheric H_2O absorption feature regions are in blue. Al-OH, Fe-OH, and Mg-OH absorption feature regions are in green, brown, and orange, respectively.

EM7 was identified as a mixture of pipes and minerals (mainly kaolinite). This was mainly dust. In Figure 15, the only colored area is a dusty concrete block on the leach pad. This shows that the results for this endmember are not very accurate. Compared to other endmembers, EM7 has strong fluctuations in the whole spectrum and few definite features except for kaolinite near 2200 nm and between 2300 nm and 2400 nm.

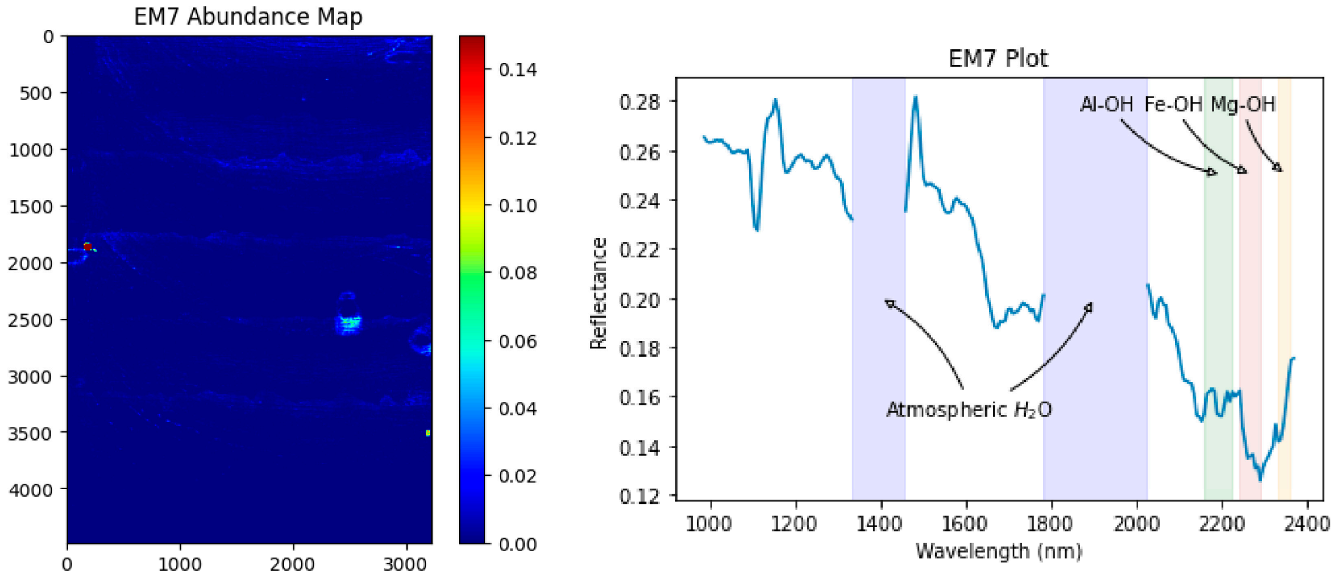

Figure 15. The spatial distribution of EM7 (**left**). Plot of the spectrum (EM7) from NFINDR (**right**). Atmospheric H_2O absorption feature regions are in blue. Al-OH, Fe-OH, and Mg-OH absorption feature regions are in green, brown, and orange, respectively.

EM8 is also similar to EM2 and -5 and was identified as mostly irrigation pipes with a little montmorillonite. However, EM8 was affected by noise and artificial problems, which is obvious at 2350 nm (Figure 16).

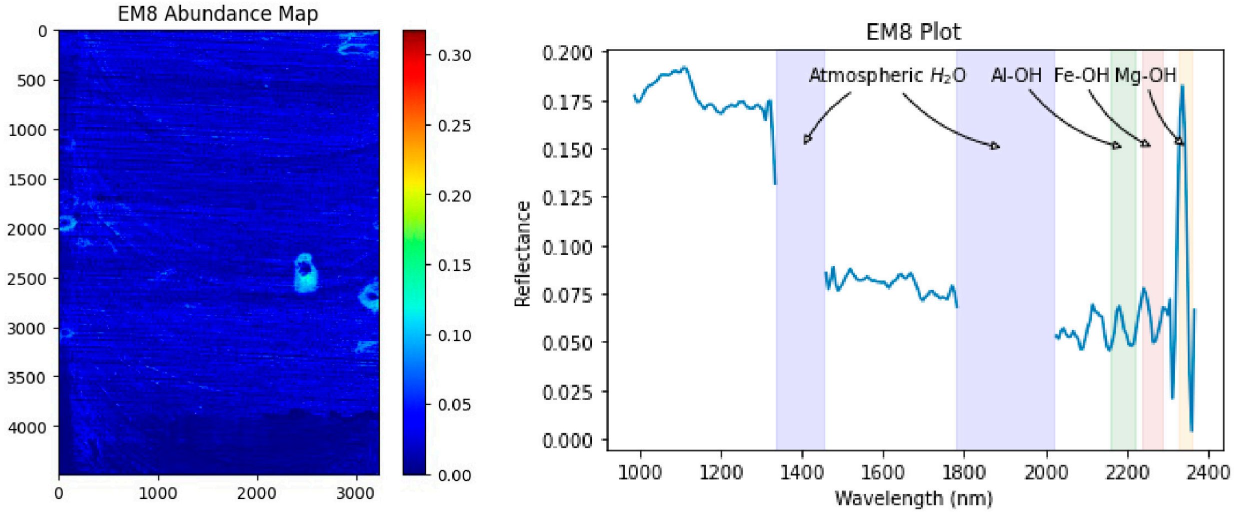

Figure 16. The spatial distribution of EM8 (**left**). Plot of the spectrum (EM8) from NFINDR (**right**). Atmospheric H_2O absorption feature regions are in blue. Al-OH, Fe-OH, and Mg-OH absorption feature regions are in green, brown, and orange, respectively.

EM9 was identified as a wet precipitate with a little muscovite and diopside. Muscovite has a feature at 2114 nm, diagnostic single sharp Al-OH absorption at 2180–2228 nm, and a doublet feature at 2342 nm and 2435 nm. However, the doublet feature is hard to detect in this spectrum due to noise. Compared with enstatite, diopside lacks the broad feature near 1900 nm but has a diagnostic feature at 1040 nm related to ferrous iron (Figure 17).

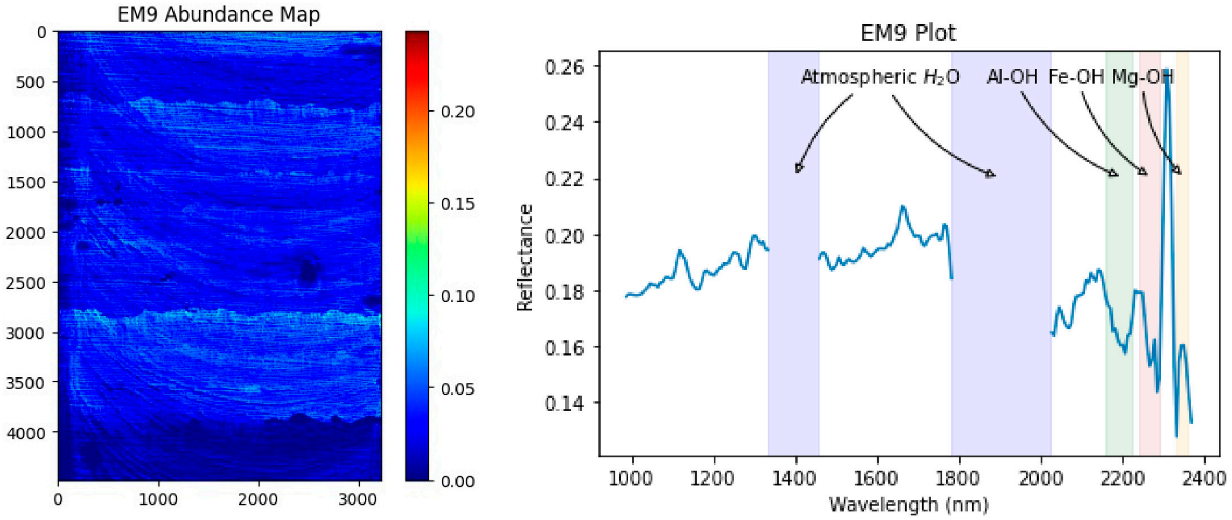

Figure 17. The spatial distribution of EM9 (**left**). Plot of the spectrum (EM9) from NFINDR (**right**). Atmospheric H_2O absorption feature regions are in blue. Al-OH, Fe-OH, and Mg-OH absorption feature regions are in green, brown, and orange, respectively.

EM10 was identified as a wet precipitate with clinochlore and minor epidote. Clinochlore is a type of Mg-chlorite, with features described above. Epidote has three features at 1545 nm, 2256 nm, and 2335–2342 nm (Figure 18).

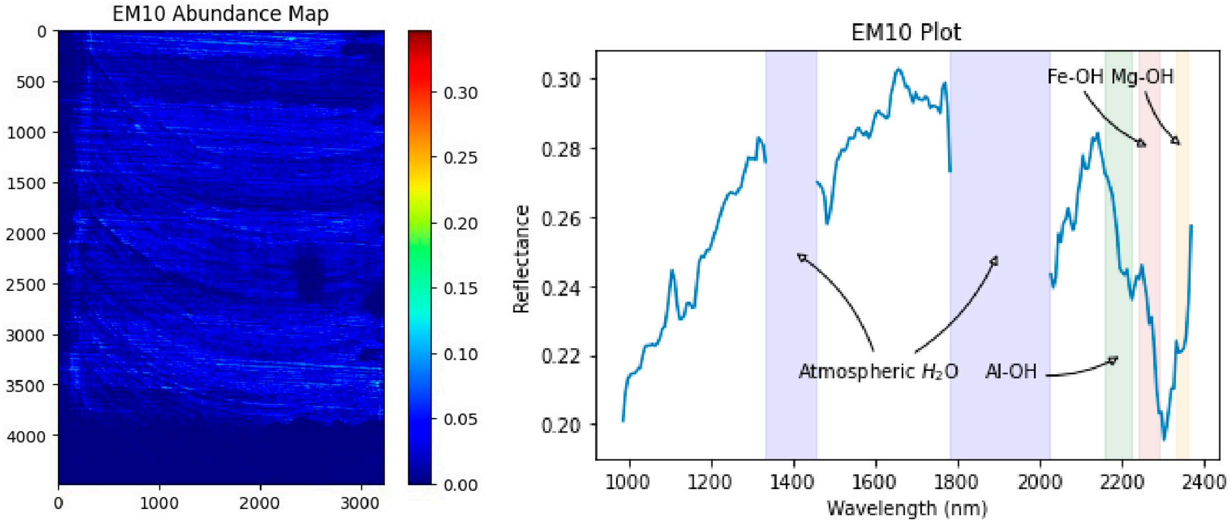

Figure 18. The spatial distribution of EM10 (**left**). Plot of the spectrum (EM10) from NFINDR (**right**). Atmospheric H_2O absorption feature regions are in blue. Al-OH, Fe-OH, and Mg-OH absorption feature regions are in green, brown, and orange, respectively.

There are some inaccuracies in identification in this method. Endmembers 3 and 4 both have a large proportion of water, but their abundance maps do not reflect the lixiviant ponds on the leach pad. EM7 was identified as mostly irrigation pipes, but its abundance map does not exhibit any irrigation pipes. Almost all the maps show abrupt changes in abundance with flight directions and stitching lines, which is not realistic. Further, the detection of enstatite is not consistent with the mineralogy of this area.

The inaccuracies in identification are mainly due to the quality of the data. The data from flight scanning were noisy to start with. The spectra from the leach pad had high concentrations of water, which dampens the reflectance of everything else. The materials on the leach pad were mixtures, which cause shifts in spectral features. The ores were crushed and agglomerated, meaning most of the ores were coated by fine-grain minerals, further shifting spectral features. All of these led to poor quality of data and misidentification of endmembers.

5.4. Discussion of Endmember Abundance Maps

Although misidentifications exist, the abundance maps of some endmembers indeed provide some information. EM1 shows the moisture distribution on the leach pad, which helps to detect lixiviant ponds on the leach pad (Figure 9). The moisture content can indirectly reflect the irrigation rate and permeability of leach pads. The irrigation rate can be adjusted based on the water distribution in different cells and modules instead of just monitoring the lixiviant flow. For instance, when the moisture content is always high in a module, then the irrigation rate should be reset to a lower value. If the abundance map of moisture (EM1) shows a lot of red areas, which indicate lixiviant ponds, metallurgists should be aware of the low permeability of the leach pad and an excessive irrigation rate. They should check their database for the size of ore, clay content, and irrigation rate of these areas. Before they start the next lift, they can strip deeper in the lixiviant pond areas. Lixiviant ponds not only represent low permeability of leach pads but also indicate high pore pressure of leach pads, which can cause geotechnical problems. Geotechnical groups should check the piezometers, inclinometers, and InSAR report of leach pads.

EM2, -5, and -8 represent irrigation pipes on the leach pad. The horizontal lines are clear in Figures 10, 13 and 16, which can be used to indicate the status of irrigation pipes on leach pads. This information provides data for mining companies to monitor pipe status. For example, if the round shape (precipitates) in the precipitates' map becomes bigger and the discontinuous pipelines in the abundance map are faded or the gaps between them become larger, it shows that the pipes are worn out or plugged.

5.5. Abundance Maps of Ground Truth Library

The results from data processing on the red pathway are shown below.

Due to the endmembers not being reliably identified and the effect of sulfuric acid and water on the spectra, directly using the ground truth library to unmix the dataset might be a better choice. Figures 19–34 are the results from the red pathway of FCLS unmixing with reference libraries (Figure 1). We found that the red pathway procedure also captured information such as horizontal pipelines, mineral distribution along stacker lines, and montmorillonite around the lixiviant ponds. The abundances of materials on the leach pad are more reasonable. The most abundant component is water and the second most abundant is sulfate, because ores are agglomerated by highly concentrated sulfuric acid and leached by sulfuric acid after stacking them. Water also represents some dark minerals which absorb incident light and do not have any spectral features. Some minerals such as quartz, plagioclase, and orthoclase are not spectrally active in VNIR and SWIR. They were added into the libraries because they can contribute to spectra, if we assume spectra are the linear combination of materials' reflectance. Adding the species might help us to obtain more accurate abundances of spectrally active minerals.

Compared with extracting endmembers, FCLS unmixing with reference libraries worked better as the abundances of minerals were more accurate. Table 5 shows the abundances of key minerals on the leach pad. The survey report was provided by the mining company. The XRD analysis was performed on the crushed rock samples and does not reliably distinguish clays.

Although the abundances are different between the two methods, the material distributions are similar. The key minerals, such as chlorite and montmorillonite, are distributed along stacker lines and near lixiviant ponds. Both methods captured water and sulfate content all over the leach pad. Horizontal lines representing the irrigation pipes were also captured in the corresponding abundance maps.

Table 5. The abundances of minerals from survey, XRD analysis, and tested methods.

Minerals	Survey	XRD	Black Pathway (N-FINDR)	Red Pathway (General Library)
Biotite	7–10%	7–10%	~3%	~7%
Chlorite	4–7%	3–7%	~2%	~5%
Kaolinite	2–3%	-	~1%	~3%
Muscovite	5–10%	3–5%	~0%	~6%
Montmorillonite	7–9%	-	~4%	~10%

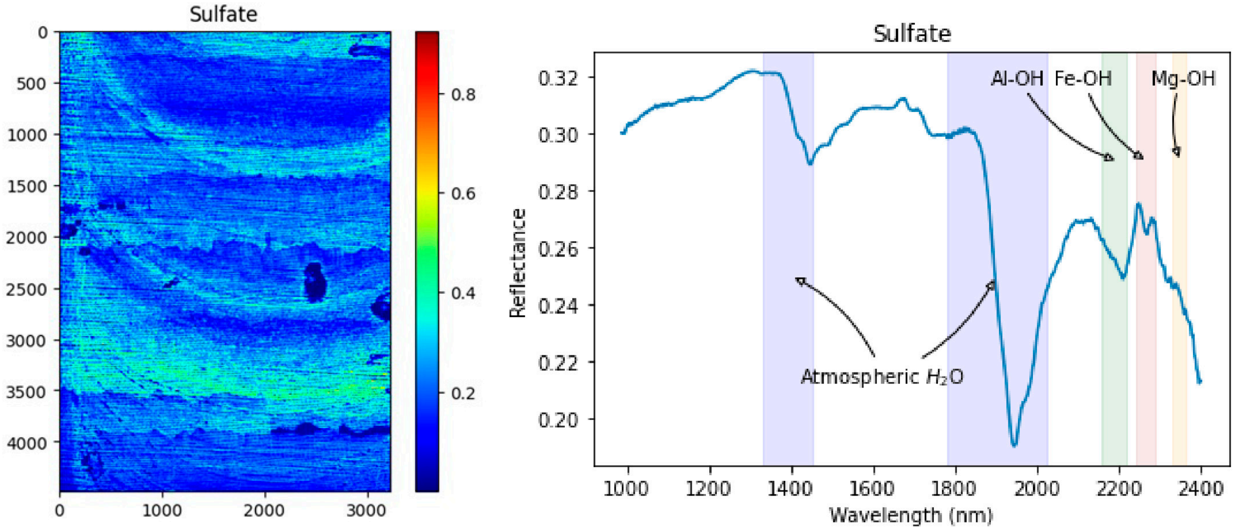

Figure 19. The spatial distribution of sulfate (**left**). Plot of sulfate spectrum extracted from precipitation samples (**right**). Atmospheric H_2O absorption feature regions are in blue. Al-OH, Fe-OH, and Mg-OH absorption feature regions are in green, brown, and orange, respectively.

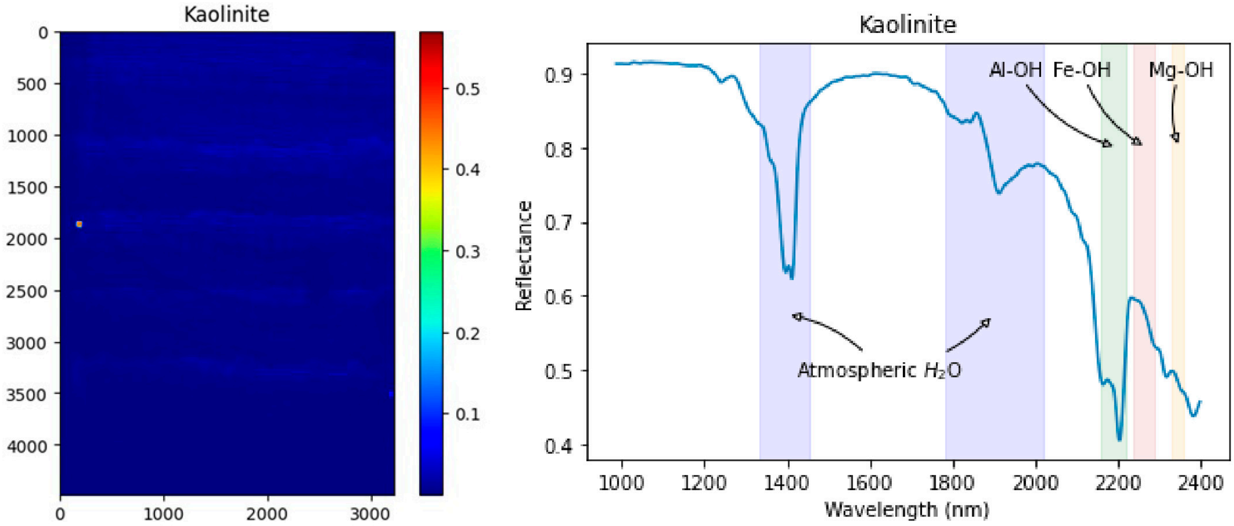

Figure 20. The spatial distribution of kaolinite (**left**). Plot of the kaolinite spectrum from the USGS library (**right**). Atmospheric H_2O absorption feature regions are in blue. Al-OH, Fe-OH, and Mg-OH absorption feature regions are in green, brown, and orange, respectively.

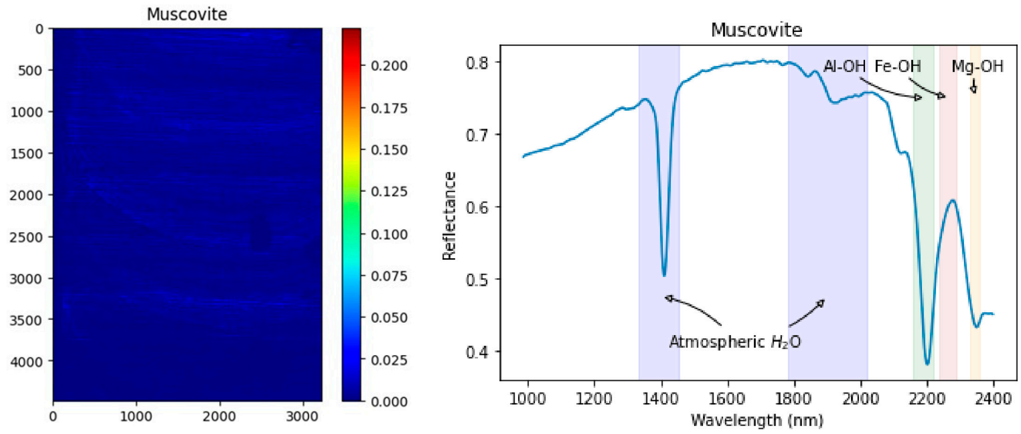

Figure 21. The spatial distribution of muscovite (**left**). Plot of the muscovite spectrum from the USGS library (**right**). Atmospheric H_2O absorption feature regions are in blue. Al-OH, Fe-OH, and Mg-OH absorption feature regions are in green, brown, and orange, respectively.

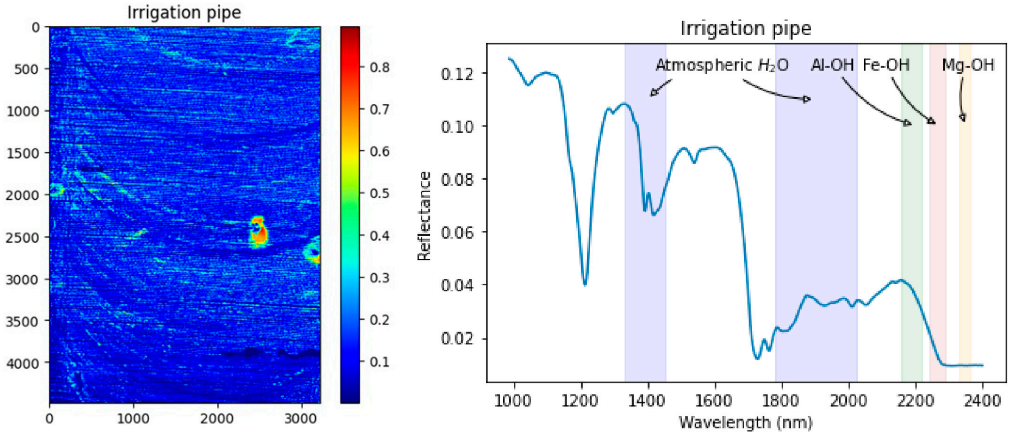

Figure 22. The spatial distribution of irrigation pipes (**left**). Plot of the irrigation pipe spectrum extracted from pipes on the leach pad (**right**). Atmospheric H_2O absorption feature regions are in blue. Al-OH, Fe-OH, and Mg-OH absorption feature regions are in green, brown, and orange, respectively.

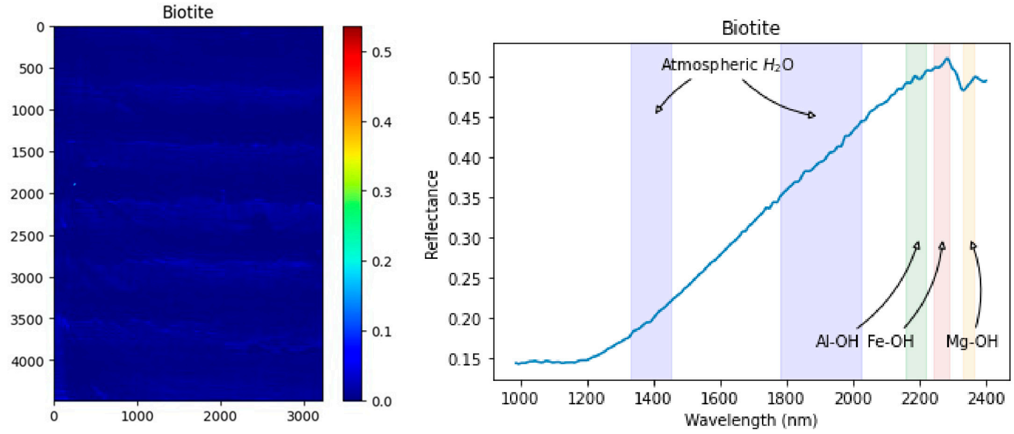

Figure 23. The spatial distribution of biotite (**left**). Plot of the biotite spectrum from the USGS library (**right**). Atmospheric H_2O absorption features regions are in blue. Al-OH, Fe-OH, and Mg-OH absorption feature regions are in green, brown, and orange, respectively.

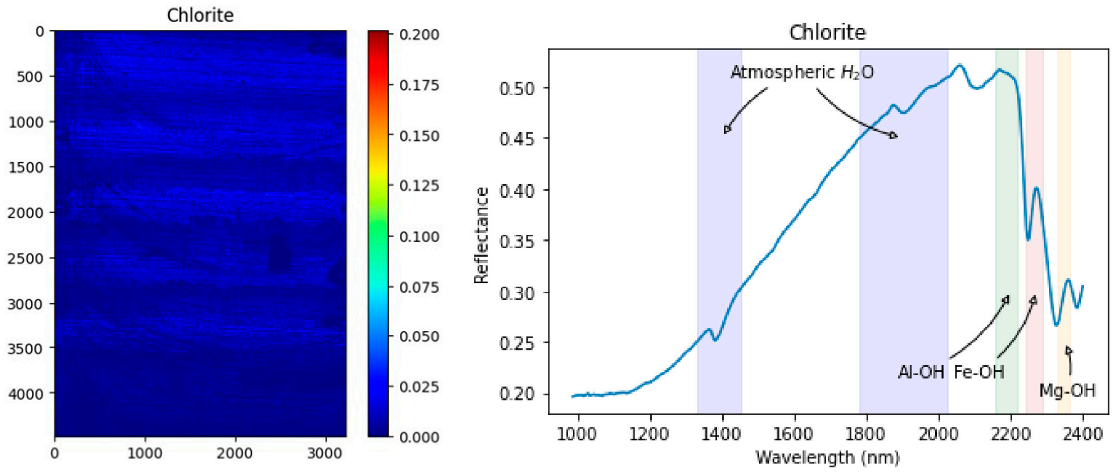

Figure 24. The spatial distribution of chlorite (**left**). Plot of the chlorite spectrum from the USGS library (**right**). Atmospheric H_2O absorption feature regions are in blue. Al-OH, Fe-OH, and Mg-OH absorption feature regions are in green, brown, and orange, respectively.

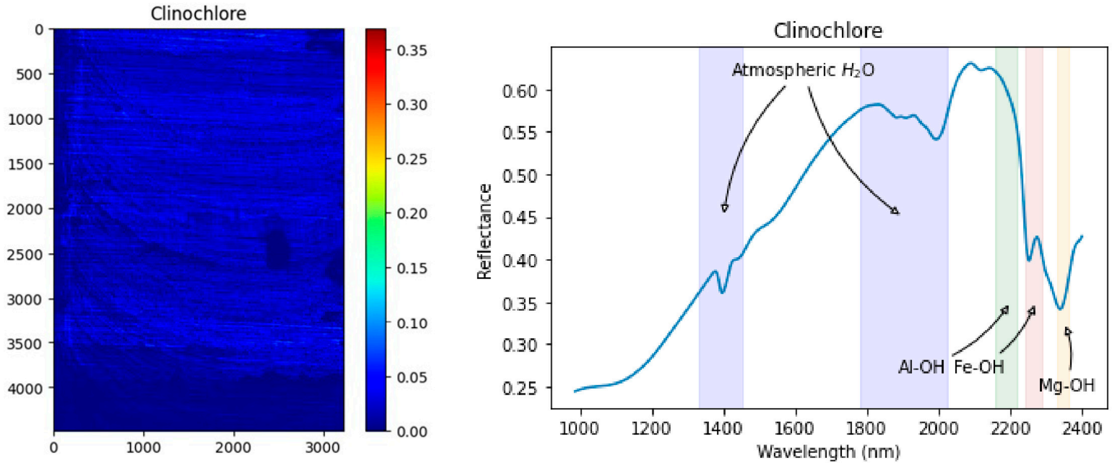

Figure 25. The spatial distribution of clinochlore (**left**). Plot of the clinochlore spectrum from the USGS library (**right**). Atmospheric H_2O absorption feature regions are in blue. Al-OH, Fe-OH, and Mg-OH absorption feature regions are in green, brown, and orange, respectively.

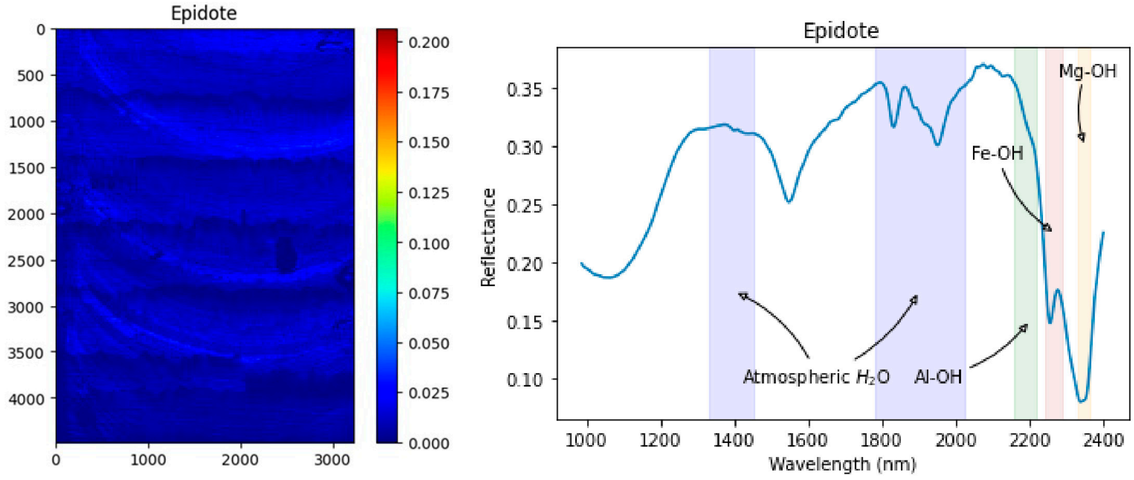

Figure 26. The spatial distribution of epidote (**left**). Plot of the epidote spectrum from the USGS library (**right**). Atmospheric H_2O absorption feature regions are in blue. Al-OH, Fe-OH, and Mg-OH absorption feature regions are in green, brown, and orange, respectively.

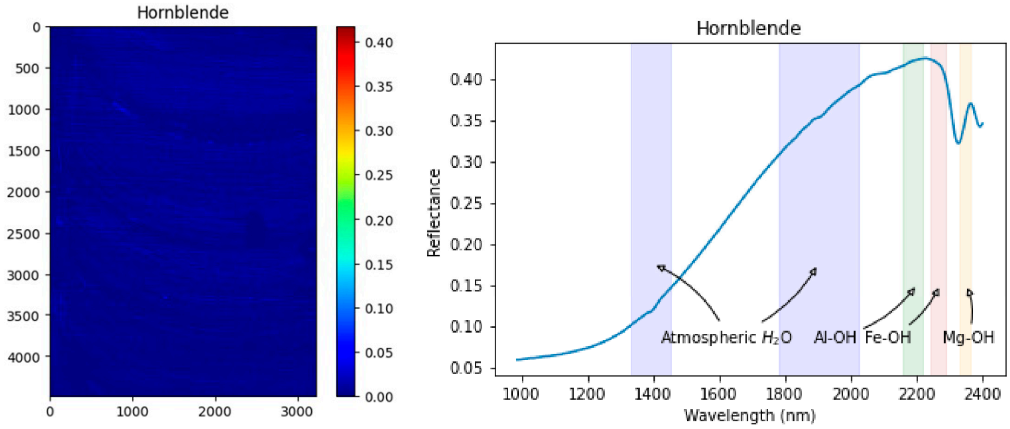

Figure 27. The spatial distribution of hornblende (**left**). Plot of the hornblende spectrum from the USGS library (**right**). Atmospheric H_2O absorption feature regions are in blue. Al-OH, Fe-OH, and Mg-OH absorption feature regions are in green, brown, and orange, respectively.

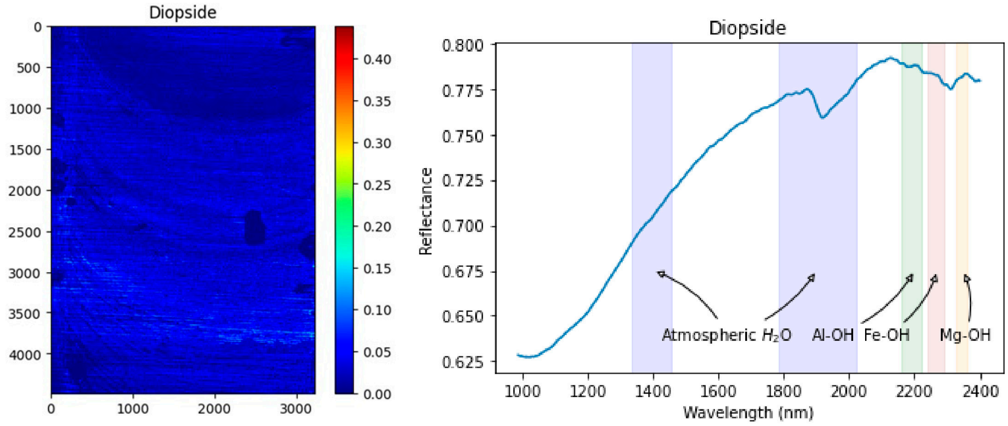

Figure 28. The spatial distribution of diopside (**left**). Plot of the diopside spectrum from the USGS library (**right**). Atmospheric H_2O absorption feature regions are in blue. Al-OH, Fe-OH, and Mg-OH absorption feature regions are in green, brown, and orange, respectively.

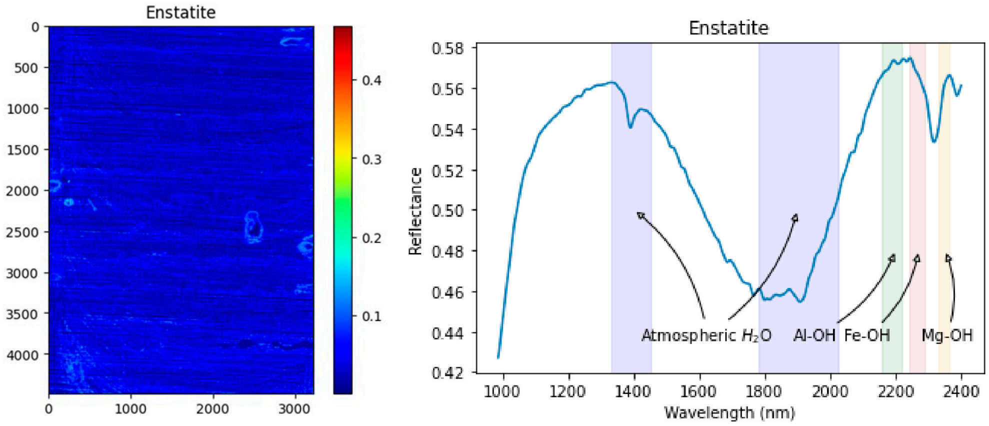

Figure 29. The spatial distribution of enstatite (**left**). Plot of the enstatite spectrum from the USGS library (**right**). Atmospheric H_2O absorption feature regions are in blue. Al-OH, Fe-OH, and Mg-OH absorption feature regions are in green, brown, and orange, respectively.

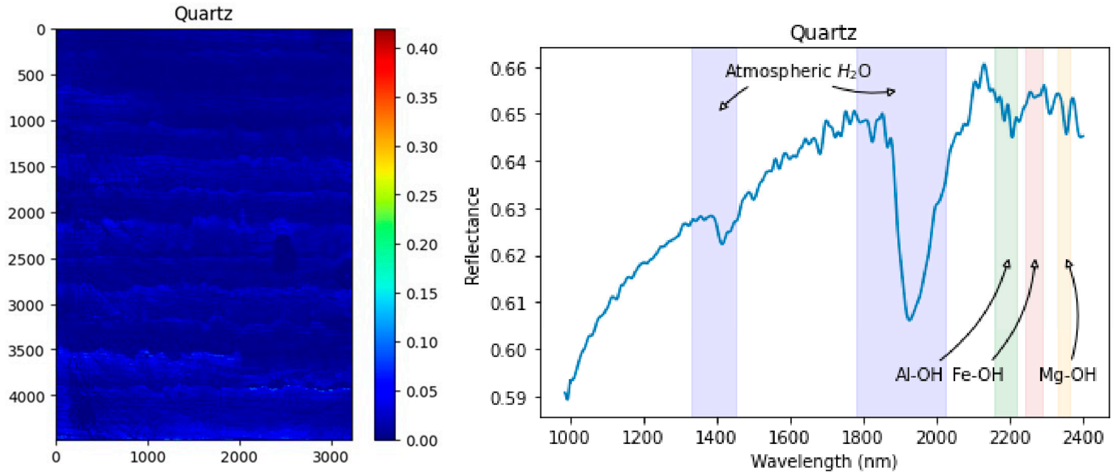

Figure 30. The spatial distribution of quartz (**left**). Plot of the quartz spectrum from the USGS library (**right**). Atmospheric H_2O absorption feature regions are in blue. Al-OH, Fe-OH, and Mg-OH absorption feature regions are in green, brown, and orange, respectively.

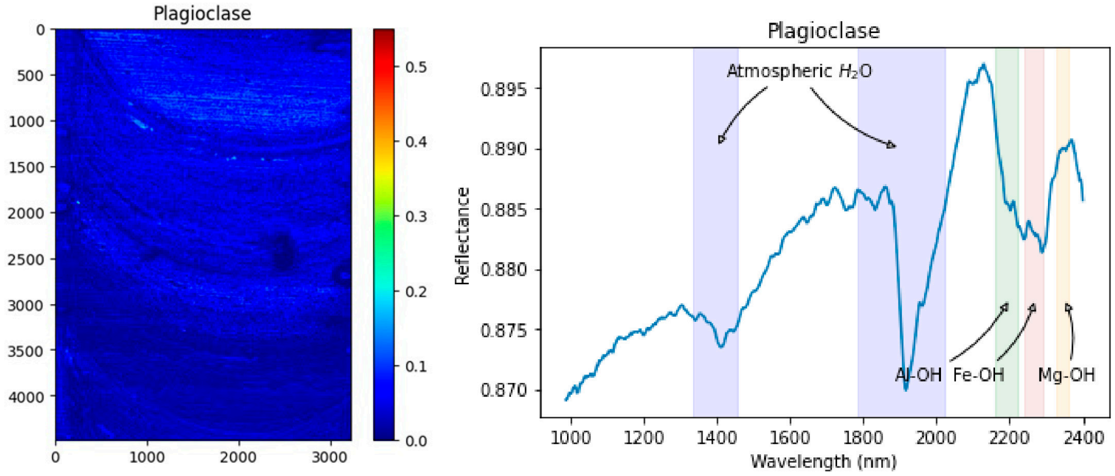

Figure 31. The spatial distribution of plagioclase (**left**). Plot of the plagioclase spectrum from the USGS library (**right**). Atmospheric H_2O absorption feature regions are in blue. Al-OH, Fe-OH, and Mg-OH absorption feature regions are in green, brown, and orange, respectively.

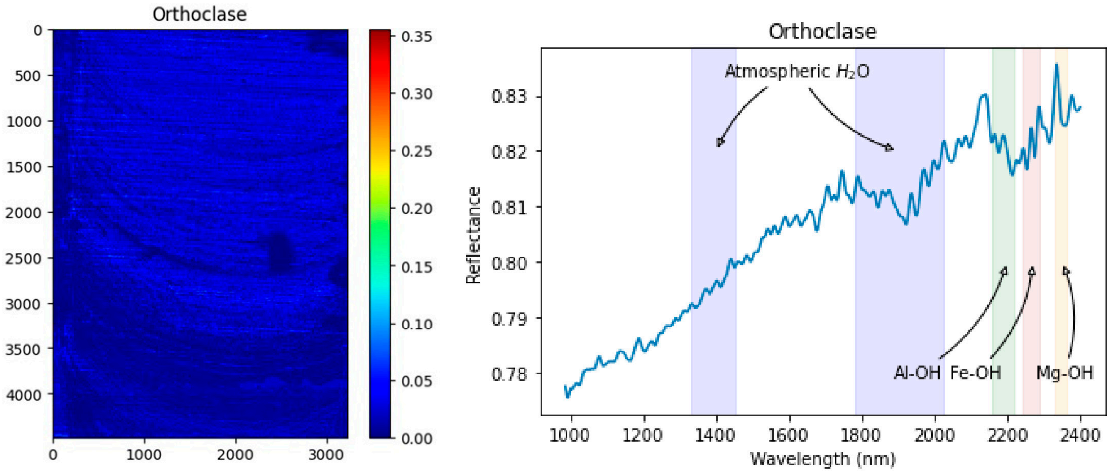

Figure 32. The spatial distribution of orthoclase (**left**). Plot of the orthoclase spectrum from the USGS library (**right**). Atmospheric H_2O absorption feature regions are in blue. Al-OH, Fe-OH, and Mg-OH absorption feature regions are in green, brown, and orange, respectively.

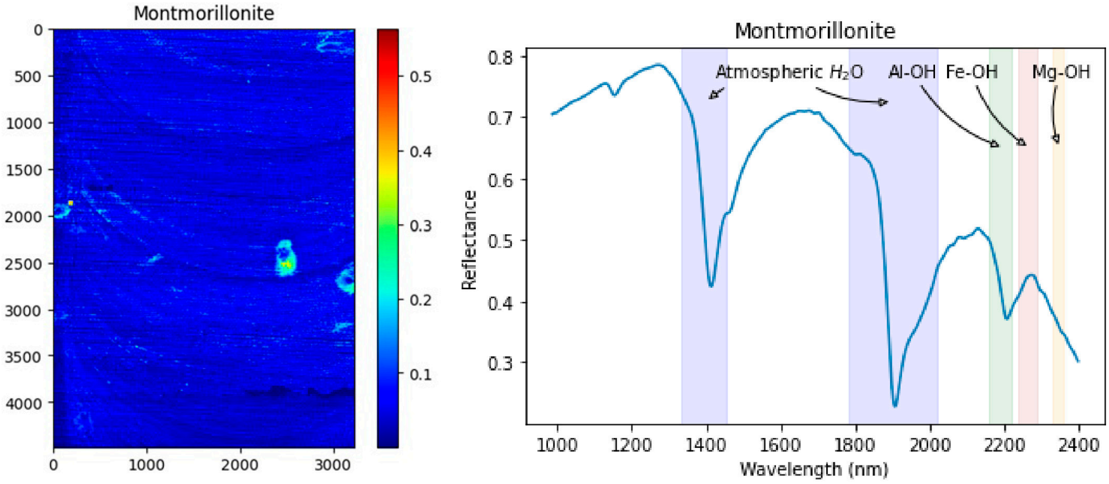

Figure 33. The spatial distribution of montmorillonite (**left**). Plot of the montmorillonite spectrum from the USGS library (**right**). Atmospheric H_2O absorption feature regions are in blue. Al-OH, Fe-OH, and Mg-OH absorption feature regions are in green, brown, and orange, respectively.

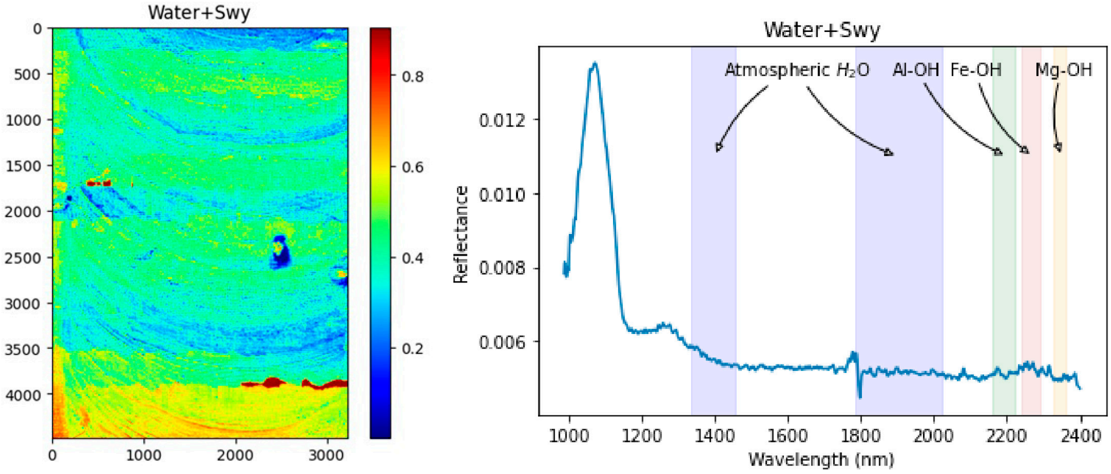

Figure 34. The spatial distribution of water (**left**). Plot of the water spectrum from the USGS library (**right**). Atmospheric H_2O absorption feature regions are in blue. Al-OH, Fe-OH, and Mg-OH absorption feature regions are in green, brown, and orange, respectively.

There are some differences between both sets of abundance maps, the XRD report, and the mining company’s mineralogy survey. The probable reason is that the ores on the leach pad were soaked by sulfuric acid, the ongoing chemical reactions changed the components, and water dampened the spectra. In addition, the ores were also crushed into small pieces, agglomerated with highly concentrated sulfuric acid, and coated with fine-grained particles. This can cause wavelength shifts. Generally speaking, the spectra changed a lot due to crushing and agglomeration.

5.6. Comparison

Both methods tested in this study assumed that the pixels in the hyperspectral image were mixtures, which is consistent with the situation on the leach pad. However, they have some differences that make the red pathway (without endmember extraction) more suitable for metallurgical applications, even though it does not include the conventional steps of virtual dimensionality and endmember extraction. As we can see, virtual dimensionality is not reliable when datasets are mixtures and homogenized by external factors (crushing, agglomeration, and leaching) because virtual dimensionality depends on variance and the noise/signal ratio. Endmember extraction also depends on variance. When the spectra of materials are similar, endmember extraction will pay attention to the variance between noise and signals instead of variance between features in the spectra. However, endmember extraction and virtual dimensionality work well in situations where spectra are distinctive such as land coverage, ocean coasts, and burned areas. These techniques are still used widely in ecology and environmental engineering. The black pathway (with endmember extraction) is also a good method for other applications in mining environments, such as drill core scanning and swelling clay detection. These are lab-based scans rather than field-based scans, which can provide lower noise and more distinctive features of minerals, which maximize the advantages of endmember extraction.

Compared with the black pathway, the red pathway is also more convenient. It directly unmixes the dataset with pure mineral references without virtual dimensionality and endmember extraction, which saves processing time. It also avoids contamination of endmembers because endmembers are not extracted from the image data. That is why this method works better when data are noisy and spectra are similar. However, it has some disadvantages. The red pathway mainly relies on prior knowledge, determined by experts who studied the imaged areas. This limits the area that can be imaged and processed by this method. It also requires a specific library which can be matched with spectra in the image.

6. Conclusions

Figuring out the health condition of leach pads is a challenging problem for mining companies. Hyperspectral imaging is a potential tool for metallurgists to monitor leach pads. However, the best practices for analyzing hyperspectral data from leach pads have not been explored. Compared with the common applications of hyperspectral remote sensing, hyperspectral imaging on leach pads might require unconventional steps. This study tested a popular step in spectral analysis, N-FINDR, to figure out if endmember extraction is necessary when monitoring leach pads with hyperspectral imaging. This manuscript also suggests how to use hyperspectral images to monitor leach pads.

The results show that hyperspectral imaging systems can directly measure some parameters, such as clay content and moisture distribution. However, the unmixing results with endmembers show that N-FINDR identified unrealistic amounts of water and minerals. The results with a reference library are more realistic, but there are some problems in both methods. The water contents are too high in both sets of results, and the spectrally inactive minerals are treated as water in the linear mixture model. Compared with traditional methods for testing clay content, both techniques are more effective and provide continuous map data, which are useful for monitoring leach pads. However, FCLS and matching with a reference library is more suitable than FCLS and endmember extraction for analyzing data from leach pads. When datasets are noisy and full of mixtures, avoiding endmember extraction can increase the processing speed and accuracy.

Author Contributions: Conceptualization, I.B. and D.N.R.; methodology, D.N.R.; validation, I.B., D.N.R. and J.H.; formal analysis, J.H.; resources, I.B.; writing—original draft preparation, J.H.; writing—review and editing, I.B.; visualization, J.H. and D.N.R.; supervision, I.B.; project administration, I.B.; funding acquisition, I.B. All authors have read and agreed to the published version of the manuscript.

Funding: This research was funded by SME Foundation and Freeport-McMoRan (unnumbered grants).

Data Availability Statement: The data is unavailable due to privacy.

Conflicts of Interest: The authors declare no conflict of interest.

References

1. Plaza, A.; Martínez, P.; Pérez, R.; Plaza, J. A quantitative and comparative analysis of endmember extraction algorithms from hyperspectral data. *IEEE Trans. Geosci. Remote Sens.* **2004**, *42*, 650–663. [CrossRef]
2. Veganzones, M.A.; Grana, M. Endmember extraction methods: A short review. In Proceedings of the International Conference on Knowledge-Based and Intelligent Information and Engineering Systems, Zagreb, Croatia, 3–5 September 2008.

3. Vishnu, S.; Nidamanuri, R.R.; Bremananth, R. Spectral material mapping using hyperspectral imagery: A review of spectral matching and library search methods. *Geocarto Int.* **2013**, *28*, 171–190. [CrossRef]
4. Shanmugam, S.; SrinivasaPerumal, P. Spectral matching approaches in hyperspectral image processing. *Int. J. Remote Sens.* **2014**, *35*, 8217–8251. [CrossRef]
5. Hiskey, J.B. Current status of U.S. gold and silver heap leaching operations, heap and dump leaching practice. In Proceedings of the 1983 SME Fall Meeting, Salt Lake City, UT, USA, 19–31 October 1983.
6. Kappes, D. Precious metal heap leach design and practice. In *Mineral Processing Plant Design, Practice and Control*; SME: Englewood, CO, USA, 2002.
7. Bartlett, R. *Solution Mining: Leaching and Fluid Recovery of Materials*; Routledge: London, UK, 1998.
8. He, J.; DuPlessis, L.; Barton, I. Heap leach pad mapping with drone-based hyperspectral remote sensing at the Safford Copper Mine, Arizona. *Hydrometallurgy* **2022**, *211*, 105872. [CrossRef]
9. Van Der Meer, F. Analysis of spectral absorption features in hyperspectral imagery. *Int. J. Appl. Earth Obs. Geoinf.* **2004**, *5*, 55–68. [CrossRef]
10. Polidori, E. Relationship between the Atterberg limits and clay content. *Soils Found.* **2007**, *47*, 887–896. [CrossRef]
11. Zhang, S.; Liu, W. Application of aerial image analysis for assessing particle size segregation in dump leaching. *Hydrometallurgy* **2017**, *171*, 99–105. [CrossRef]
12. Tang, M.; Esmaeili, K. Heap leach pad surface moisture monitoring using drone-based aerial images and convolutional neural networks: A case study at the El Gallo Mine, Mexico. *Remote Sens.* **2021**, *13*, 1420. [CrossRef]
13. Daud, O.; Correa, M.; Estay, H.; Ruíz-del-Solar, J. Monitoring and controlling saturation zones in heap leach piles using thermal analysis. *Minerals* **2021**, *11*, 115. [CrossRef]
14. Rucker, D.; Schindler, A.; Levitt, M.; Glaser, D. Three-dimensional electrical resistivity imaging of a gold heap. *Hydrometallurgy* **2009**, *98*, 267–275. [CrossRef]
15. Ren, H.; Zhao, Y.; Xiao, W.; Hu, Z. A review of UAV monitoring in mining areas: Current status and future perspectives. *Int. J. Coal Sci. Technol.* **2019**, *6*, 320–333. [CrossRef]
16. Ilankoon, I.; Cole, K.; Neethling, S. Measuring hydrodynamics dispersion coefficients in unsaturated packed beds: Comparison of PEPT with conventional tracer tests. *Chem. Eng. Sci.* **2013**, *89*, 152–157. [CrossRef]
17. Ilankoon, I.; Neethling, S.; Huang, Z.; Cheng, Z. Improved inter-particle flow models for predicting heap leaching hydrodynamics. *Miner. Eng.* **2017**, *111*, 108–115. [CrossRef]
18. Ilankoon, I.; Neethling, S. Inter-particle liquid spread pertaining to heap leaching using UV fluorescence based image analysis. *Hydrometallurgy* **2019**, *183*, 175–185. [CrossRef]
19. Fischer, C.; Kakoulli, I. Multispectral and hyperspectral imaging technologies in conservation: Current research and potential applications. *Stud. Conserv.* **2006**, *51* (Suppl. S1), 3–16. [CrossRef]
20. Van der Meer, F.; Van der Werff, H.; Van Ruitenbeek, F.; Hecker, C.; Bakker, W.; Carranza, J. Multi- and hyperspectral geologic remote sensing: A review. *Int. J. Appl. Earth Obs. Geoinf.* **2012**, *14*, 112–128. [CrossRef]
21. Feng, Y.Z.; Sun, D.W. Application of Hyperspectral Imaging in Food Safety Inspection and Control: A Review. *Crit. Rev. Food Sci. Nutr.* **2012**, *52*, 1039–1058. [CrossRef] [PubMed]
22. Calin, M.A.; Parasca, S.V.; Savastru, D.; Manea, D. Hyperspectral Imaging in the Medical Field: Present and Future. *Appl. Spectrosc. Rev.* **2014**, *49*, 435–447. [CrossRef]
23. Wang, B.; Sun, J.; Xia, L.; Liu, J.; Wang, Z.; Li, P.; Guo, Y.; Sun, X. The Applications of Hyperspectral Imaging Technology for Agricultural Products Quality Analysis: A Review. *Food Rev. Int.* **2023**, *39*, 1043–1062. [CrossRef]
24. Clark, R. Spectroscopy of rocks and minerals, and principles of spectroscopy. In *Manual of Remote Sensing*; John Wiley and Sons, Inc.: New York, NY, USA, 1999; pp. 3–58.
25. He, J.; Barton, I. Hyperspectral remote sensing for detecting geotechnical problems at Ray mine. *Eng. Geol.* **2021**, *292*, 106261. [CrossRef]
26. Peyghambari, S.; Zhang, Y. Hyperspectral remote sensing in lithological mapping, mineral exploration, and environmental geology: An updated review. *J. Appl. Remote Sens.* **2021**, *15*, 031501. [CrossRef]
27. Bedini, E. The use of hyperspectral remote sensing for mineral exploration: A review. *J. Hyperspectr. Remote Sens.* **2017**, *7*, 189–211. [CrossRef]
28. Krupnik, D.; Khan, S. Close-range, ground-based hyperspectral imaging for mining applications at various scales: Review and case studies. *Earth-Sci. Rev.* **2019**, *198*, 102952. [CrossRef]
29. Murphy, R.; Schneider, S.; Monteiro, S. Mapping layers of clay in a vertical geological surface using hyperspectral imagery: Variability in parameters of SWIR absorption features under different conditions of illumination. *Remote Sens.* **2014**, *6*, 9104–9129. [CrossRef]
30. Schneider, S.; Murphy, R.; Monteiro, S.; Nettleton, E. On the development of a hyperspectral library for autonomous mining systems. In Proceedings of the Australiasian Conference on Robotics and Automation, Sydney, Australia, 2–4 December 2009.
31. Meyer, J.; Kokaly, R.; Holley, E. Hyperspectral remote sensing of white mica: A review of imaging and point-based spectrometer studies for mineral resources, with spectrometer design considerations. *Remote Sens. Environ.* **2022**, *275*, 113000. [CrossRef]

32. Thiele, S.; Bnoulkacem, Z.; Lorenz, S.; Bordenave, A.; Menegoni, N.; Madriz, Y.; Dujoncquoy, E.; Gloaguen, R.; Kenter, J. Mineralogical mapping with accurately corrected shortwave infrared hyperspectral data acquired obliquely from UAVs. *Remote Sens.* **2021**, *14*, 5. [CrossRef]
33. Notesco, G.; Ogen, Y.; Ben-Dor, E. Integration of hyperspectral shortwave and longwave infrared remote-sensing data for mineral mapping of Makhtesh Ramon in Israel. *Remote Sens.* **2016**, *8*, 318. [CrossRef]
34. Kopačková, V. Using multiple spectral feature analysis for quantitative pH mapping in a mining environment. *Int. J. Appl. Earth Obs. Geoinf.* **2014**, *28*, 28–42. [CrossRef]
35. Zabcic, N.; Rivard, B.; Ong, C.; Müller, A. Using airborne hyperspectral data to characterize the surface pH and mineralogy of pyrite mine tailings. *Int. J. Appl. Earth Obs. Geoinf.* **2014**, *32*, 152–162. [CrossRef]
36. Freeport-McMoRan. *FMI 2022 10-K Report*; Freeport-McMoRan: Phoenix, AZ, USA, 2022.
37. Robinson, R.; Cook, A. The Safford Copper Deposit, Lone Star Mining District, Graham County, Arizona. In *Geology of the Porphyry Copper Deposits of Southwestern North America*; University of Arizona Press: Tucson, AZ, USA, 1966; pp. 251–266.
38. Langton, J.; Williams, S. Structural, Petrological and Mineralogical Controls for the Dos Pobres Orebody Lone Star Mining District, Graham County, Arizona. In *Advances in Geology of the Porphyry Copper Deposits Southwestern North America*; University of Arizona Press: Tucson, AZ, USA, 1982; pp. 335–352.
39. The University of Arizona College of Science. The Arizona Geological Survey. Available online: https://geomapaz.azgs.arizona.edu/ (accessed on 23 May 2024).
40. AusSpec. *Spectral Interpretation Field Manual*; AusSpec International Pty: Otago, New Zealand, 2008.
41. Coulter, D.; Harris, P.; Wickert, L.; Zhou, X. Adcances in spectral geology and remote sensing: 2008–2017. *Exploration* **2017**, *17*, 23–50.
42. Barreto, M.A.P.; Johansen, K.; Angel, Y.; McCabe, M.F. Radiometric Assessment of a UAV-Based Push-Broom Hyperspectral Camera. *Sensors* **2019**, *19*, 4699. [CrossRef] [PubMed]
43. Savitzky, A.; Golay, M. Smoothing and differentiation of data by simplified least squares procedures. *Anal. Chem.* **1964**, *36*, 1627–1639. [CrossRef]
44. Pearson, K. On lines and planes of closest fit to systems of points in space. *Philos. Mag. A* **1901**, *6*, 559–572. [CrossRef]
45. Rodarmel, C.; Shan, J. Principal component analysis for hyperspectral image classification. *Surv. Land Inf. Sci.* **2002**, *62*, 115–122.
46. Bioucas-Dias, J.; Nascimento, J. Hyperspectral subspace identification. *IEEE Trans. Geosci. Remote Sens.* **2008**, *46*, 2435–2445. [CrossRef]
47. Winter, M. N-FINDR: An Algorithm for Fast Autonomous Spectral End-Member Determination in Hyperspectral Data. In Proceedings of the Imaging Spectrometry V, Denver, CO, USA, 19–21 July 1999.
48. Heinz, D.; Chang, C.; Althouse, M. Fully constrained least-squares based linear unmixing [hyperspectral image classification]. In Proceedings of the IEEE 1999 International Geoscience and Remote Sensing Symposium, Hamburg, Germany, 28 June–2 July 1999.
49. Tian, J.; Philpot, W. Relationship between surface soil water content, evaporation rate, and water absorption band depths in SWIR reflectance spectra. *Remote Sens. Environ.* **2015**, *169*, 280–289. [CrossRef]
50. Moshtaghi, M.; Knaeps, E.; Sterckx, S.; Meire, D. Spectral reflectance of marine macroplastics in the VNIR and SWIR measured in a controlled environment. *Sci. Rep.* **2021**, *11*, 5436. [CrossRef]
51. Cloutis, E.; Hawthorne, F.; Mertzman, S.; Krenn, K.; Craig, M.; Marcino, D.; Methot, M.; Strong, J.; Mustard, J.; Blaney, D.; et al. Detection and discrimination of sulfate minerals using reflectance spectroscopy. *Icarus* **2006**, *184*, 121–157. [CrossRef]